Princeton Plasma Physics Laboratory

PPPL- 4600

PPPL- 4600

Calculation of the Non-Inductive Current Profile in High-Performance NSTX Plasmas

S.P. Gerhardt, E. Fredrickson, D. Gates, S. Kaye, J. Menard, M.G. Bell, R.E. Bell, B.P. LeBlanc, H. Kugel, S.A. Sabbagh, and H. Yun

February, 2011

PPPL
PRINCETON PLASMA PHYSICS LABORATORY

Prepared for the U.S. Department of Energy under Contract DE-AC02-09CH11466.

Princeton Plasma Physics Laboratory
Report Disclaimers

Full Legal Disclaimer

Trademark Disclaimer

PPPL Report Availability

Princeton Plasma Physics Laboratory:

http://www.pppl.gov/techreports.cfm

Office of Scientific and Technical Information (OSTI):

http://www.osti.gov/bridge

Related Links:

U.S. Department of Energy

Office of Scientific and Technical Information

Fusion Links

Calculation of the Non-Inductive Current Profile in High-Performance NSTX Plasmas

S.P. Gerhardt[1], E. Fredrickson[1], D. Gates[1], S. Kaye[1], J. Menard[1], M. G. Bell[1], R. E. Bell[1], B.P. Le Blanc[1], H. Kugel[1], S. A. Sabbagh[2], H. Yuh[3]

1: Princeton Plasma Physics Laboratory
2: Columbia University
3: Nova Photonics

Keywords: NSTX, Spherical Torus, Neutral Beam Current Drive, Bootstrap Current
PACS Numbers: 52.55.Fa, 52.55.Tn, 52.55.Wq

Abstract

The constituents of the current profile have been computed for a wide range of high-performance plasmas in NSTX [M. Ono, et al., Nuclear Fusion **40**, 557 (2000)]; these include cases designed to maximize the non-inductive fraction, pulse length, toroidal-β, or stored energy. In the absence of low-frequency MHD activity, good agreement is found between the reconstructed current profile and that predicted by summing the independently calculated inductive, pressure-driven, and neutral beam currents, without the need to invoke any anomalous beam ion diffusion. Exceptions occur, for instance, when there are toroidal Alfven eigenmode avalanches or coupled m/n=1/1+2/1 kink-tearing modes. In these cases, the addition of a spatially and temporally dependent fast ion diffusivity can reduce the core beam current drive, restoring agreement between the reconstructed profile and the summed constituents, as well as bringing better agreement between the simulated and measured neutron emission rate. An upper bound on the fast ion diffusivity of ~0.5-1 m^2/sec is found in "MHD-free" discharges, based on the neutron emission, time rate of change of the neutron signal when a neutral beam is stepped, and reconstructed on-axis current density.

1: Introduction

The spherical torus [1] has been proposed as the fusion core for devices designed to test high heat flux plasma material interactions [2], study fusion nuclear science (FNS) [3-7], or generate electricity [8,9]. The interest in this configuration was spawned from theoretical work like that discussed in Ref. [1]. The first larger experimental test of the ST was the START [10] device, which achieved values of toroidal β exceeding 30% [11,12] under neutral beam (NB) heating [13]. These results lead to further theoretical studies of the achievable equilibria for the ST [14,15], producing configurations with virtually 100% of the toroidal current provided by the pressure-driven bootstrap current [16-20]; these configurations were stable to both high-n ballooning and n=1-3 kink modes (with a nearby conducting wall). The START results, along with these theory developments, motivated the construction of the I_P=1 MA class STs NSTX (National Spherical Torus Experiment) [21] and MAST (Mega-Ampere Spherical Torus) [22]. Results from these two devices have then paved the way for the design of the next step devices noted above.

Part of the design process for these next-step spherical torii is to define the shape and magnitude of the toroidal current density profile, and specify the current drive tools that will provide that current. The designers assume that the current profile can be predicted as the sum of pressure driven currents, neutral beam driven currents, currents driven by radio frequency and microwave means, and potentially some residual inductive current. It is the purpose of this paper to study the make-up of these different toroidal current sources in a wide variety of high-performance plasmas in the National Spherical Torus Experiment (NSTX).

Calculation of the individual components of the current profile is a well-established process in conventional aspect ratio tokamaks. The inductive current is calculated from the surface voltage profile [23] and neoclassical resistivity [24]. The bootstrap current can be calculated from simple analytic models such as those in Refs. [24,25], or multi-species models as in the NCLASS code [26]. The neutral beam current [27-33] is often calculated from Monte Carlo codes, with NUBEAM [34,35] a

commonly used example. Code packages also exist to calculate the current driven by RF and microwave current drive tools. Calculations of this sort have been applied to most large tokamaks, with an incomplete list including DIII-D [23, 36-51], JET [52-56], JT-60 [57,58], TFTR [59], and ASDEX-Upgrade [60]. These calculations have often assumed classical physics for the beam ions, though there are cases where this assumption may not be warranted. For instance, tearing modes have been shown to modify the neutral beam current profile [37,42], consistent with observations of fast ion loss due to these instabilities [61,62]. Alfven modes have also been shown to modify the current profile [63,64]. Recently, evidence from DIII-D [49,50] and ASDEX-Upgrade [60] has indicated that the electrostatic turbulence responsible for thermal plasma transport may also lead to radial diffusion of the injected fast ions.

Calculations of this sort are less well established in the spherical torus configuration. Experiments in MAST [65] used upward and downward shifted L-mode plasmas in order to study off-axis neutral beam current drive. The off-axis NBCD helped avoid harmful MHD instabilities, and extended the operational window for the device. At lower injected powers (P_{inj}<2 MW), TRANSP [66] simulations of the neutron rate and stored energy agreed well with measurement. When the neutral beam power was increased, fishbone modes were observed, and an *ad hoc* fast ion diffusivity was required in TRANSP to match the measured neutron emission rate and stored energy.

A first assessment of the current profile constituents in high-β NSTX H-mode plasmas was published in Refs. [67,68]. Ref. 67 examined a single discharge in detail. It showed that in the absence of low-frequency MHD, the reconstructed current profile could indeed be understood as the sum of neoclassical pressure driven currents, inductive currents, and beam driven currents, with purely (neo)classical physics for all calculations. During the later phase of the discharge, an m/n=1/1 rotating core MHD mode grew and saturated; anomalous fast ion diffusion was required to understand the current profile reconstruction during this phase. A similar calculation was reported in Ref. [69], where good agreement was found between the current profile reconstructed from Grad-Shafranov solutions and that

summed from calculations of the current profile constituents; only a small discrepancy in the on-axis current density was reported. Calculations of the non-inductive fraction in NSTX using TRANSP and NUBEAM have also been reported in Refs. [70-73]. These studies used kinetic profiles as inputs to the code, and showed good matches between the measured and simulated neutron emission, but did not have the detailed analysis and crosschecking of the current profile described here.

This paper focuses on two important questions, expanding on the previous MAST and NSTX papers in a number of important ways. First, under what conditions can the NSTX current profile be understood as the sum of neoclassical current drive sources? Second, what is the effect of some typical MHD events on the fast ion driven current, and what is the upper bound on the fast ion diffusivity in discharges that do not have low-frequency MHD?

The current profile composition is studied for a range of high-performance discharges over a wide range of q_{95} (q_{95} is the safety factor at the magnetic surface that encloses 95% of the enclosed poloidal flux); these include high-q_{95}, high-β_P discharges optimized for highest non-inductive fraction, medium-q_{95} cases optimized for long pulse, and low-q_{95} cases optimized for high toroidal β and/or maximal stored energy. In the high-q_{95}, high-β_P case, we evaluate discharges that are free of MHD, that have TAE avalanches, and that have coupled m/n=2/1 + 1/1 modes; the effects of these modes on the current profile is addressed. The upper bound for anomalous fast ion diffusivity in plasmas without low-frequency MHD is discussed. Overall, the results of this paper are cautiously optimistic with respect to current profile prediction using neoclassical physics only; however, a number of issues that may complicate this conclusion are discussed.

The remainder of this paper is organized as follows. Section 2 describes the NSTX device and analysis techniques that are used. Section 3 examines the evolution of the neutron emission rate when the neutral beams are stepped on and off, by comparing the measured evolution to that predicted by the NUBEAM module within TRANSP. Section 4 studies the reconstruction of the current profile from constituent parts, for a series of high-q_{95}, high-β_P discharges designed to maximize the non-

inductive fraction. The effects of TAE avalanches and rotating n=1 kink/tearing modes on the current profile are illustrated. Section 5 describes similar analysis of a discharge optimized for maximum pulse length. Section 6 describes current profile analysis for discharges designed to maximize the toroidal β and stored energy. Section 7 contains a discussion of an upper bound on the fast-ion diffusivity in MHD-free discharges. Section 8 contains a discussion and summary of these results.

2: The NSTX device and Analysis Techniques

NSTX [21] is a medium size spherical torus designed to test the benefits of extending the traditional tokamak to low aspect ratio [1]. The geometric major radius of a typical high-β plasma is $R_0 \approx 0.85$m, with a Shafranov-shifted magnetic axis radius of 1.05-1.1 m. The minor radius is typically 60 cm, yielding typical aspect ratios R_0/a of 1.3-1.5. The plasma currents from discharges in this paper span the typical NSTX operating space of $0.7 < I_P\,(\mathrm{MA}) < 1.3$; toroidal field strengths up to 0.55T are available, though this paper addresses discharges with $0.4 < |B_T|\,(\mathrm{T}) < 0.48$. The plasmas in this paper are heated with up to 6 MW of co-injected neutral beam power, and all have β_N values at or above the n=1 no-wall limit. The neutral beam (NB) injection system is composed of a single beamline with three independent NB sources. These sources are referred to as sources A, B, and C, with tangency radii of approximately 70, 60, and 50 cm respectively. Further information regarding the neutral beam geometry can be found in Ref. [74].

The discharges in this paper were generally optimized to push a high-performance boundary, such as highest non-inductive fraction, longest possible pulse, or highest stored energy. These goals are generally facilitated by running with high-elongation (κ) and high-triangularity (δ) [75,76]. This is illustrated in the plasma cross-section for high-β_P discharge 133964 in Fig. 1. Note that the shape control in NSTX is provided by a combination of realtime equilibrium reconstruction and plasma boundary control with an "ISOFLUX" algorithm [77]. Also, dynamic error field correction (DEFC) of n=1 error fields [78], static correction of n=3 error fields [79] and fast RWM control [80,81] are important for improving the overall

stability and reliability of these discharge scenarios. The stability and transport properties of these discharges, and comparison to previously developed high-performance NSTX plasmas, is discussed in Ref. [82].

Lithium conditioning of the graphite plasma facing components is used for all plasmas described in this paper. Two lithium evaporators deposit lithium vapor on the vessel floor; this lithium primarily coats the divertor, and to a lesser extent, the center column and lower passive plates [83,84]. This conditioning has many beneficial effects, including the elimination of ELMs [85], reduction of electron transport [86] and the lowering of the H-mode threshold [87]. The elimination of ELMs, however, typically leads to an uncontrolled accumulation of impurities [84], including metals and carbon from the plasma facing components. Note that these lithium induced changes can affect the non-inductive current drive in a number of ways. For comparable density, the higher T_e increases the fast ion slowing down time (and thus the beam current drive), while also increasing the pressure and bootstrap fraction, since $f_{BS} \propto \beta_P$. The higher Z_{eff} increases the beam current drive (see eqn 2 below), though at the expense of lower β compared to a plasma with similar electron content and lower Z_{eff}. The detailed study of these lithium effects is, however, outside the scope of the present paper.

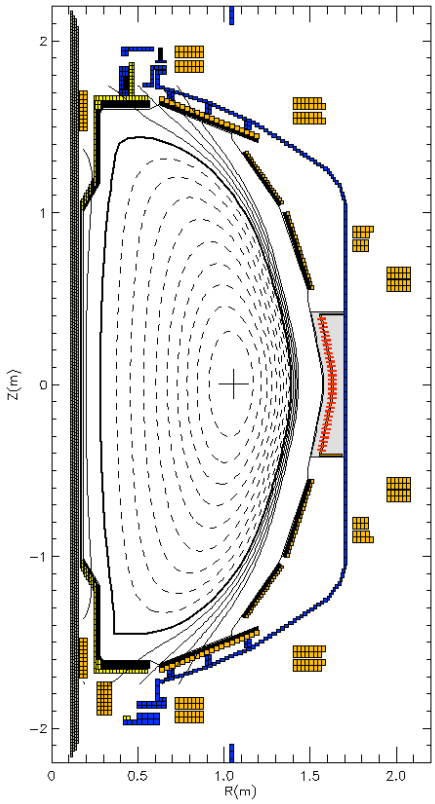

Fig. 1) Plasma cross-section for the discharge with lowest flat-top average loop voltage of any H-mode NB heated discharge in NSTX (133964). This discharge will be studied in detail in Sects. 4, 7, and 8. The shape is typical of the discharges described in this paper.

The comprehensive NSTX diagnostic set is of critical importance in deriving the results in this paper. The electron temperature and density are measured by a 30 point Thomson scattering system [88] with measurement points along the midplane on both sides of the magnetic axis. The ion temperature, carbon concentration, and carbon toroidal velocity are measured by a 51 channel charge exchange recombination spectroscopy (CHERS) diagnostic measuring primarily on the outboard midplane; the deuterium profile is then inferred from the electron and carbon density profiles using quasi-neutrality and the assumption that no additional impurities are present. The magnetic field pitch angle is measured by a 16 channel motional Stark effect (MSE) diagnostic [89].

As implied above, the primary analysis method in this paper is composed of three steps. The first step is to "reconstruct" the plasma current profile from Grad-

Shafranov solutions that are constrained to match the available data. The second step is to compute the profiles of the inductive, neutral beam, and pressure driven currents from the reconstructions and measured plasma profiles. This third step is to sum these current profile constituents, and compare the sum to the reconstructed current density.

The Grad-Shafranov solutions in this paper are calculated with the code LRDFIT [90]. All such reconstructions shown in this paper are constrained by the external magnetics, diamagnetic flux measurement, E_R corrected MSE measurements, and a T_e isotherm requirement (that is, solutions found by the code are constrained to have the same temperature on both the inside and outside of the magnetic surface at the midplane). The code is run to two different ways. The first method uses a version of the Grad-Shafranov equation with rotational corrections to the equilibrium, and is indicated in this paper by the text "LRDFIT09" in the figures. In other cases, we have solved the traditional Grad-Shafranov equation without rotation, but with an additional constraint on the pressure profile; these are indicated by the text "LRDFIT12". In these cases, the measured total kinetic pressure, from Thomson scattering and CHERS, is used to constraint the MHD pressure profile in the outer 1/3 of the plasma, where the fast ion pressure should be small; this provides a very strong constraint on the pedestal height and edge current density. The pressure profile over the inner 2/3 of the plasma is not constrained, since we do not know, within the confines of this code, the fast ion pressure profile. We have generally favored the "09" runs, as they converge more easily. However, we have found that the "12" runs are sometimes required in order reconstruct details in the profile shapes.

The time-series of reconstructions so computed is then used to calculate the toroidal electric field $E_\phi = \frac{d\psi}{dt}\Big/ R$ and loop voltage $V_{loop} = \frac{2\pi\left\langle E_\varphi B_\varphi \right\rangle}{F\left\langle R^{-2}\right\rangle}$. The parallel inductive current density is then computed as $\frac{\left\langle J_\parallel B\right\rangle_{ind}}{\left\langle B\cdot\nabla\phi\right\rangle} = \sigma_{neoc}\frac{V_{loop}}{2\pi}$, where σ_{neoc} is computed from the Sauter formulation [24]. Here, ψ is the poloidal flux.

The relevant pressure driven currents include the toroidal components of the Pfirsch-Schlueter and diamagnetic currents [19] and the bootstrap currents [16-20, 25]. The latter is a neoclassical current that has the potential to provide most or all of the current required to sustain the tokamak equilibrium. Simplistically, it can be understood as the parallel current that must flow to cancel the poloidal part of the perpendicular (diamagnetic) current, since poloidal currents are strongly damped by viscosity due to the field variation in that direction [20]. The beneficial effect of stronger toroidal field (TF) can be understood in this picture by observing that as the TF is increased, a larger part of the perpendicular currents will be in the poloidal direction, and larger parallel current must flow in order to have a substantial poloidal component. The particular formulation of the bootstrap current used in this paper is presented in Ref. [24,91], and can be expressed as

$$\langle J_{\parallel} B \rangle = F(\psi) p_e \left(L_{31} A_1 + L_{32} A_2 + L_{34} A_4 \right) \qquad [1]$$

where the A_i are functions of the kinetic profile gradients as

$$A_1 = \frac{1}{p_e}\frac{\partial p_e}{\partial \psi} + \frac{1}{p_e}\frac{\partial p_i}{\partial \psi}$$

$$A_2 = \frac{1}{T_e}\frac{\partial T_e}{\partial \psi}, \quad A_2^i = \frac{1}{T_i}\frac{\partial T_i}{\partial \psi}$$

$$A_4 = \alpha \frac{1 - R_{pe}}{R_{pe}} A_2^i$$

The L_{ij} are functions of the charge number, normalized collisionality and trapped particle fraction, and are defined in Ref. [24]. The expression in [1] is evaluated using either TRANSP, or with standalone routines.

The final significant term in the NSTX current drive mix is that due to neutral beam current drive [27-33,92,93]. This current is due to toroidally circulating fast ions, and can be calculated as:

$$\langle j_{NB} \cdot B \rangle = \langle j_{f\parallel} \cdot B \rangle \left[1 - \frac{Z_B}{Z_{eff}} \left(1 - G\left(Z_{eff}, \varepsilon \right) \right) \right] \qquad [2]$$

Here, $j_{f||}$ is the fast ion current, Z_B is the charge of the injected beam ion charge, and G is a function of Z_{eff} and aspect ratio, whose most complete definition can be found

in Ref [33]. The term $\frac{Z_B}{Z_{eff}}\left(1-G\left(Z_{eff},\varepsilon\right)\right)$ accounts for electrons flowing in the opposite direction and partially cancelling the fast ion current [9,33]. We have used the NUBEAM [34,35] code within TRANSP to compute the neutral beam current drive for all cases in this paper. This code has the ability to impose both an additional "anomalous" radial diffusion and radial convection on the fast ion population, as a function of both space and time. This provision has been used to simulate the effects of various MHD modes on the fast ion population.

A few other details are worth mentioning. The error bars in most figures are calculated from the standard deviation of a given signal or calculation within the specified averaging window. Thus, they do not incorporate the effects of any systematic errors. Some sources of systematic error, including profile parameterization and centrifugal effects, are discussed in section 7. All profiles are plotted against the variable ρ_{pol}, a minor radius variable defined as $\rho_{pol}=\sqrt{\frac{\psi-\psi_{core}}{\psi_{edge}-\psi_{core}}}$.

3: Comparison of the Measured and Simulated Neutron Dynamics During Beam Steps

As noted above, the results in this paper rely heavily on TRANSP calculations of the neutral beam current. Before examining those calculations directly, it is useful to compare measurements and modeling of the neutron evolution before and after a step change in the neutral beam power. Previous experiments have studied the behavior of "dilute" populations of fast ions [32,49,50,74], including studies in NSTX L-mode plasmas [74]. The latter study showed that the prompt loss and slowing down of fast ions in those plasmas were consistent with classical behavior. This topic is revisited here in order to provide a (somewhat limited) validation of the neutral beam model in TRANSP for high-performance H-mode plasmas.

The method here is that described in Ref. [74]. The neutron emission in NSTX is dominated by beam-target reactions. The increase of the neutron emission rate R_N

(in N/sec) when a beam is turned on is fit to $\frac{dR_N}{dt} = c - \frac{R_N}{\tau_R}$. The initial rise of the neutron signal is indicative of the prompt loss rate [74]. The decay of the neutron emission when a beam is turned off is fit to $\frac{dR_N}{dt} = -\frac{R_N}{\tau_D}$, and is indicative of the thermalization and slowing down of the fast ions. In each case, both the measurement and TRANSP simulation of the neutron emission are fit in an identical manner, such that the time-scales τ_D and τ_R can be compared between simulation and experiment. All fits in this section are from MHD-free phases of the discharge, and there is no anomalous fast-ion diffusivity in any calculation.

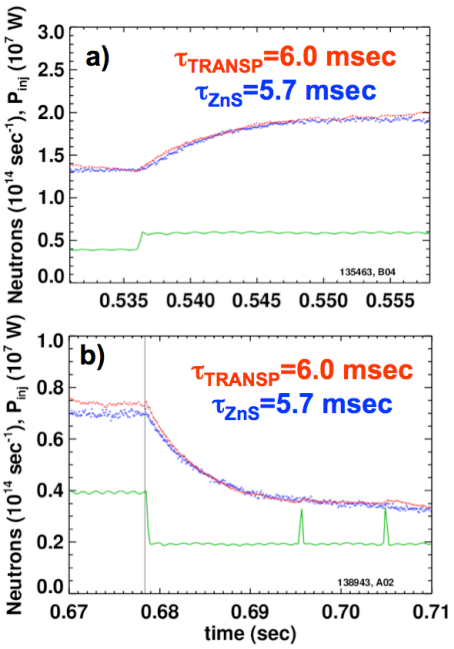

Fig. 2) Example fits to the neutron emission a) after a beam turn on, and b) after a beam turn off. The measured neutron emission is in blue, while the simulated emission is in red, and the neutral beam power is in green. The fits are shown as solid lines through the data points.

Example fits are shown in Fig. 2, for the beam turn-on in frame a), and the beam turn-off in b). The TRANSP simulations and measurements are in excellent agreement, for both the absolute magnitude of the emission and the time-scale of the change, and the model equations fit the measurement and simulations quite well.

This process has been repeated for a large number of discharges where neutral beam modulations were used. Some of these were dedicated transport experiments, while others were discharges associated with the development of β_N control via neutral beam modulation. The results of these fits are shown in Fig. 3, with fits to the rise time-constant in frame a) and to the decay time-constant in frame b). Good agreement between measured and simulated values is found in both cases.

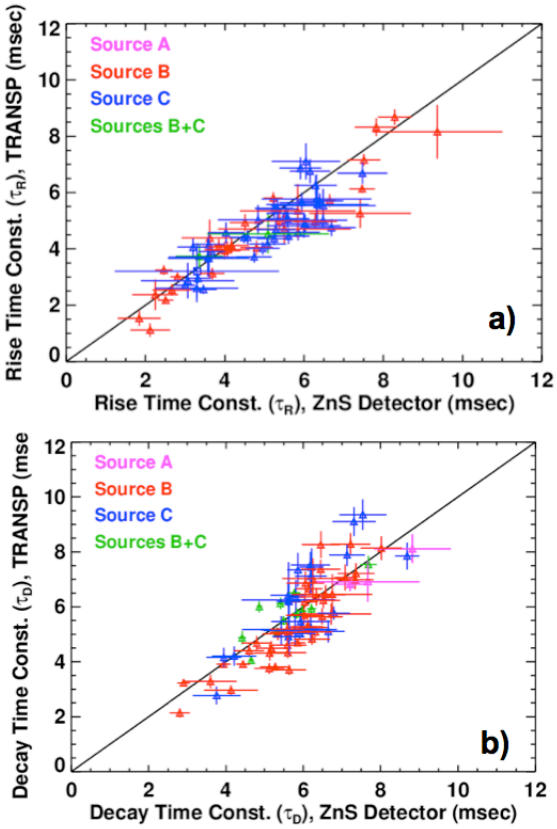

Fig. 3) Comparison of the fit time constants for measurements and TRANSP simulations. Frame a) shows the time constant associated with the beam turn-on (τ_R), while frame b) shows the time constant associated with the turn-off (τ_D)

.

The results presented here provide some validation of the NUBEAM model with TRANSP to predict the neutral beam current drive in MHD-free H-mode discharges. In particular, the neutron emission is most sensitive to the highest energy beam ions, which are also most effective at carrying the current. Also, this

comparison of measured and simulated time-scales is valid independent of any calibration factors associated with the neutron detector hardware. Note, however, that the present fast-ion D_α (FIDA) diagnostic [94], and the toroidally viewing upgrade to the system presently being designed [95], will allow much more detailed validation of the TRANSP H-mode NBCD and fast ion distribution function calculations.

4: Current Profile Reconstructions in High-q_{95}, High-β_P Plasmas Optimized for the Highest Non-Inductive Fraction

The first set of plasmas selected for study were optimized to have the highest possible non-inductive fraction, consistent with a reasonably long pulse. Since the bootstrap current increases with increasing toroidal field (see discussion in section 2), these discharges were run at a somewhat elevated toroidal field B_T=0.48 T. The TF coil heating limit at this field limits the achievable flat-top duration to ~1 second. Note that these discharges were designed to study in greater detail the high-κ scenario first described in Ref. [73].

The performance of three nearby discharges in this sequence is shown in Fig. 4.

The plasma current is 0.7 MA for all cases, as shown in frame a) and all have q_{95} of ~14; the neutral beam heating power of 6 MW (not shown) is the same in all cases as well. The MHD activity is illustrated in frame b), where the poloidal magnetic field detected at the vessel wall is processed to discriminate for odd-n signals (and is typically dominated by n=1 fluctuations). The three discharges have vastly different MHD activity, with 133958 experiencing a series of bursting MHD modes, 133959 succumbing to a large saturated n=1 mode, and 133964 exhibiting a long MHD-free period at the end of the pulse. Discharge 133964 has slightly larger fuelling and an earlier H-mode transition, both of which lead to it having higher density than the other cases.

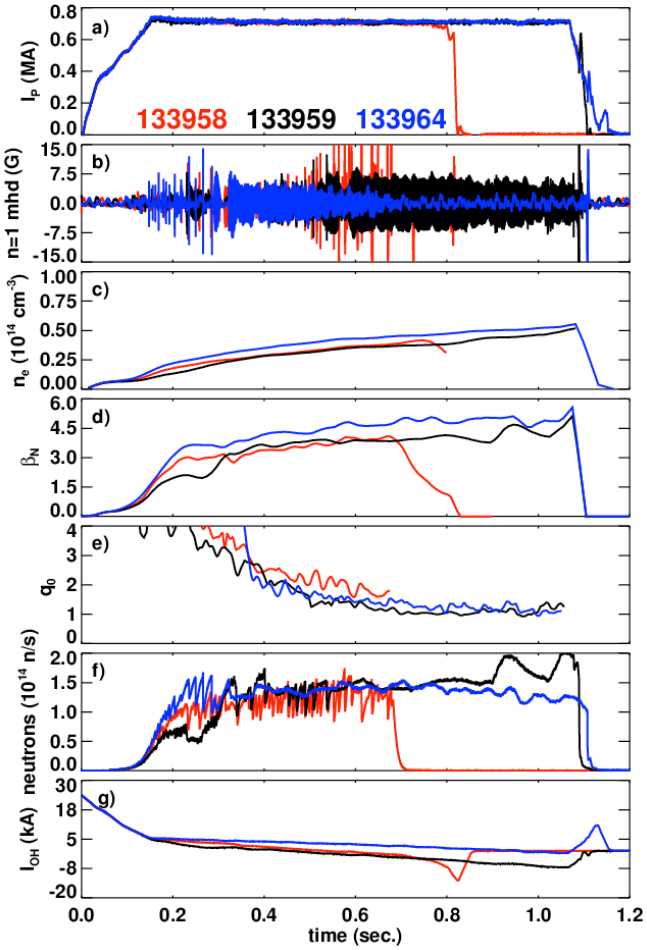

Fig. 4) Time traces of three nearly adjacent discharges, showing the different MHD activity and resulting effects. Shown are a) the plasma current, b) the Mirnov-signal processed to detect odd-n MHD, c) the line average density, d) β_N, e) the reconstructed value of q_0, and f) the neutron emission, and g) the solenoid flux consumption. All three cases are heated with 6 MW of neutral beams; the beam sources are on until the end of discharges 133959 & 133964, but turn off at t=0.67 in discharge 133958.

The discharge without low-frequency MHD (133964) also has a higher value of β_N, defined as $\beta_N = \beta_T / \left(I_P / aB_T\right)$; this is indicative of the deleterious effects of the MHD modes on the global confinement in the other cases. Interestingly, this case has a lower value of the central temperature ($T_{e,0}$=~800 eV) compared to the other cases ($T_{e,0}$=~1100-1200 eV). The temperature profile is, however, broader; when coupled to the higher density, this case has a thermal stored energy that is ~20%

higher. The TRANSP simulations described below indicate that the fast ion stored energy is 10-20% higher in 133964, despite the lower T_e and higher n_e, due to the effect of the MHD modes.

The evolution of the central safety factor is shown in frame e), and two trends are immediately apparent: i) the two discharges which last to ~1 second duration have achieved a nearly fully evolved current profile, and ii) the red case with bursting MHD modes has a substantially higher central safety factor. The measured neutron emission from the plasma is illustrated in frame f), and shows, for the red discharge, the abrupt loss of fast ions associated with the bursting MHD modes. Finally, the solenoid current is shown in frame g), as an indication of the non-inductive current behavior in these cases. Compared to the black and red cases, the blue discharge uses solenoid flux at a much reduced rate, indicating that the non-inductive fraction will be larger for this discharge. The major goal of the analysis in this section is to understand how the MHD illustrated in frame b) impacted the flux consumption indicated in frame g). These three discharges will thus be studied in the following three sub-sections.

Section 4.1: Bursting MHD Modes.

We consider first the discharge with bursting MHD modes (133958). A spectrogram of the MHD activity for this discharge is shown in Fig. 5a). There are clear overlapping bursting modes, often with simultaneous toroidal mode numbers 1 through 4. These modes have been previously identified as TAE avalanches [96,97]. There is copious evidence for the transport of fast ions due to these instabilities [97], including the sharp drops in the neutron rate noted above and from the FIDA system [94]. Simulations of these avalanches in L-mode discharges using the NOVA-K [98,99] and ORBIT [100] codes have been successful in matching the observed neutron rate drop [96].

In order to understand the effects of these modes on the current profile, we have chosen to simulate them using a temporally and spatially varying fast ion diffusivity (D_{FI}). This approach was taken for a number of reasons. For instance, the

reflectometer data used to select from among the NOVA-K eigenmodes [96] is not available in the H-mode discharges discussed here. Furthermore, even if we were to select a subset of these linear eigenfunctions, we would not have the appropriate information to scale them in order to compute the expected fast ion transport and loss. Note, however, that a beam emission spectroscopy (BES) diagnostic was recently installed on NSTX [101], which should facilitate the detailed study of these modes in H-mode plasmas.

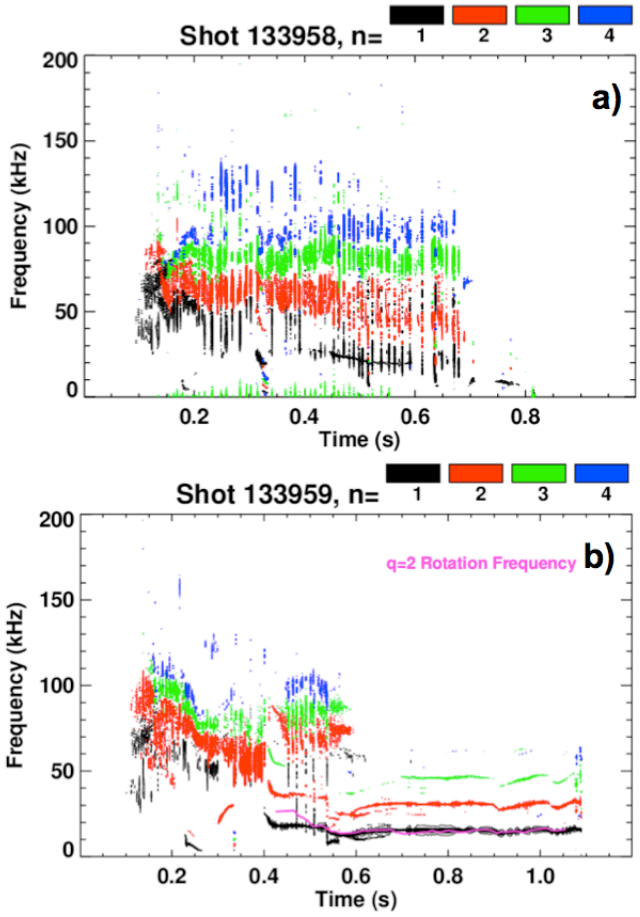

Fig. 5) Spectrograms for the two cases with strong MHD. Shown are a) 133958, with strong TAE avalanches and b) 133959, with a saturated core n=1 mode. Also shown in b) is the rotation frequency of the q=2 surface.

In order to simulate the effect of these modes on the current profile, the anomalous fast ion diffusivity radial and temporal variation was specified to TRANSP as:

$$D_{FI}\left(\rho_{pol},t\right) = \frac{A_{FI}(t)}{2}\left[1-\tanh\left(\frac{\rho_{pol}-w}{0.05}\right)\right] + D_{FI,DC}. \qquad [3]$$

This form causes the D_{FI} to be higher in the plasma core than the edge, with the width of the large-D_{FI} region determined by the parameter w. The denominator in the tanh function was always set to 0.05 to provide a smooth but reasonably sharp roll-off of D_{FI} on either side of $\rho_{pol} = w$. The temporal variation of $A_{FI}(t)$ was set by associating the start time and duration of the measured modes to the start time and duration of periods with large A_{FI}. For this experimentally determined timing, scans were done of the radial width (w) and peak amplitude of the fast ion diffusivity "bursts". The "optimal" combination of radial width and amplitude would match the average level of the neutron emission, the amplitude of the loss at each mode, and the recovery rate of the neutron emission rate between the modes. Note that for a given TRANSP run, the width and amplitude of these impulsive diffusion phases was identical, and only the timing set to match the data. Also, no effort was made to match the neutron rate drop for each mode (i.e., the parameters like A_{FI} and w were not tailored for each individual burst). The fast ion diffusivity was either set to zero or a small number for periods between the large "bursts". An example D_{FI} profile in radius and time is shown in Fig. 6a). The radial width of the D_{FI} in this case is 0.7, with peak values of 50 m^2/sec and a steady value between pulses ($D_{FI,DC}$) of 1 m^2/sec.

Given these values for the fast ion diffusivity, the results of the TRANSP calculation are shown in Fig. 6 b-e). Frame b) shows the measured neutron evolution in red. The predicted neutron emission for a TRANSP run without fast ion diffusion is shown in green, and clearly overestimates the emission while failing to capture the dynamics. The neutron emission from a TRANSP run with impulsive fast ion diffusion is shown in blue. The diffusion in this case is that in frame a) of the figure (radial width of 0.7 and amplitude of 50 m^2/sec, with 1 m^2/sec between the bursts). As will be discussed below in greater detail, the value of 1 m^2/sec between pulses is at the upper range of diffusivities that are likely for MHD-free periods. Note, however, that Fig. 5a) shows a continuous n=1 mode during the time of

analysis (0.4<t (sec) <0.6), which may explain the need for additional steady state diffusion.

The plasma stored energy is shown in frame c); here, the red trace is the "fast" stored energy from a diamagnetic loop. The green curve shows the stored energy calculated by TRANSP with no impulsive fast ion diffusion. This curve once again overestimates the measured values. The TRANSP calculation with impulsive fast ion diffusivity (in red) is much closer to the measurement. Also interesting is the similar magnitude of the stored energy drops in the fast measurement and the TRANSP calculation with impulsive fast ion diffusion.

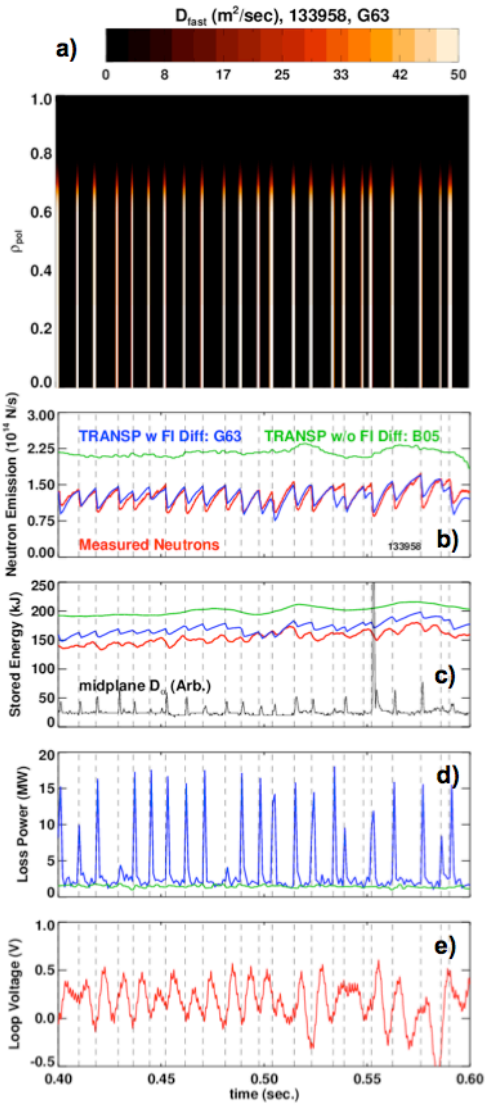

Fig. 6) Simulation of the effects of TAE Avalanches using the TRANSP+NUBEAM code. The imposed fast ion diffusion profile evolution is shown in frame a). The

time traces show b) the neutron emission, c) the stored energy, d) the calculated fast ion loss power, and e) the loop voltage. In each case, the measurement is indicated in red, a TRANSP simulation without fast ion diffusion is shown in green, and a TRANSP simulation with impulsive fast ion diffusion is shown in blue.

Frame c) also shows the D_α emission from an outboard midplane viewing chord. Each bursting mode has an associated spike in this emission, likely associated with the loss of fast ions. Similarly, the fast ion loss power computed by TRANSP is shown in frame d). The case without impulsive diffusion shows a steady loss power of ~1.5 MW, while the case with impulsive diffusion has spikes up to 15 MW. Of course, one must remember that fast ion loss modeled in TRANSP likely does not have the same energy and pitch angle dependence as that due to the actual modes. The frame is provided to show the level of transport associated with the events when these two variables are excluded.

Finally, the loop voltage is shown in frame e). This voltage is determined by a feedback loop for maintaining constant plasma current. We observe that many modes trigger an increase in loop voltage from the control system, consistent with each mode ejecting a significant fraction of the current carrying fast ions.

Many scans of the impulsive fast-ion diffusion parameters were tested in order to develop the "optimal" spatial and temporal profile shown in Fig. 6a); some of these scans are shown in Fig. 7. As noted above, the main parameters to be optimized are the radial width of the region of large diffusivity (w in Eqn. 3), and the level of diffusivity in that region (peak values of A_{FI} in Eqn. 3). The measured neutron emission, with a band indicating the standard deviation of the signal within the averaging window, is shown in gray. The key criterion in selecting the optimal D_{FI} fit dynamics is that both the average value and typical time variation match the measurement.

The red points show a scan of the impulsive diffusivity where the width of the diffusivity is limited by w=0.3. It is impossible to increase the amplitude of the impulsive diffusivity enough to match the measured neutron emission. The blue points show a scan with radial width of the large-diffusivity region given by w=0.5.

The average neutron level can be matched in this case, assuming very large impulsive values of the diffusivity (140 m^2/sec). However, the action of the modes is then too large, resulting in an overestimate of the signal variation (i.e. overestimation of the size of the neutron rate drops).

The simulation with the high-diffusivity region limited to w=0.7 (green) can match the mean value with 60-80 m^2/sec impulsive values, but also fails to match the variation. However, when "small" levels of DC diffusivity are added between the pulses, excellent agreement can be reached in the both the magnitude and variation of the neutron rate. This case with D_{FI}=1 m^2/sec between modes and spiking to 50 m^2/sec during the event results, already illustrated Fig. 6 b) & c), in a good match to both the typical crash amplitude and recovery rate after a crash.

We turn now to the implication of these modes for the current profile reconstruction. Fig. 8a) shows the current profile constituents with purely classical calculations. The neutral beam current is shown in red, the bootstrap current in blue, and the inductive current in magenta. The sum of these currents (plus the relevant component of the diamagnetic & Pfirsch-Schlueter currents) is shown in green in the figure. This green curve should be compared to the reconstructed current profile in black. Poor agreement is found between the two calculations, largely on account of the predicted large values of the central neutral beam current drive.

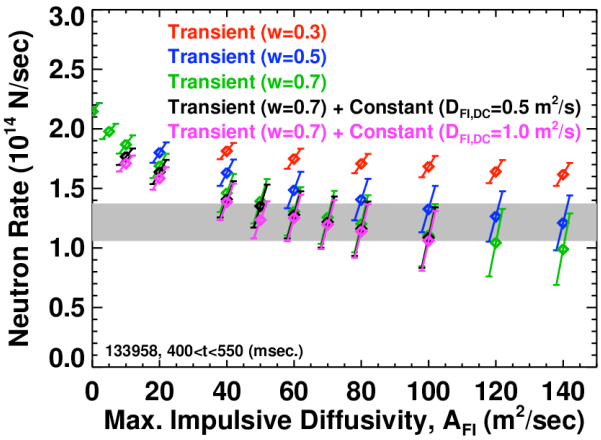

Fig. 7) Comparison of the neutron emission as a function of the amplitude of the impulsive fast ion diffusivity, for various assumptions about the profile width and diffusivity between bursts.

The situation is much improved when the neutral beam current drive is calculated including an impulsive fast ion diffusivity; the diffusivity chosen in this case is the same as that in the blue traces in Fig. 6b & c) and shown vs. radius and time in Fig. 6a). The only change in profiles for this case is the strong reduction in the beam current drive, which brings the central current density down to a value consistent with reconstructions. The various current fractions are (inductive) f_{Ind}≈45%, (pressure driven) f_{PD}≈38%, and (neutral beam) f_{NB}≈15% for this case.

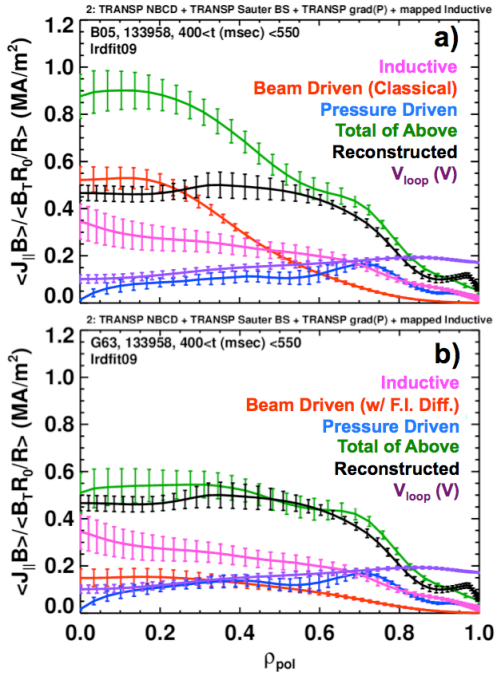

Fig. 8) Comparison of the current profile reconstruction, using a) classical collisional beam physics only, and b) the impulsive anomalous fast ion diffusivity that matches the observed neutron rate modulations and stored energy.

Section 4.2: Continuous Coupled n=1 Modes.

Next we turn to the discharge in black in Fig. 4, where a large n=1 mode is visible in frame b). The MHD mode spectrum for this discharge is shown in Fig. 5b).

A very complicated evolution of modes is observed early in the discharge, with a large series of chirping n=2 and 3 modes, accompanied after 0.4 seconds by steadily rotating n=1 modes. The chirping modes are largely eliminated by 0.55 seconds, and a large n=1 mode, with higher-n harmonics, dominates the spectrum. The frequency of this mode is an excellent match to the rotation frequency of the q=2 surface, as inferred from MSE constrained reconstructions and the CHERS data and plotted in magenta. This confirms that the underlying mode will have an important m/n=2/1 component.

Further information regarding the mode dynamics can be seen by examining the signals from a fan array of ultra-soft X-ray (USXR) signals [102]. The geometry of the array is illustrated in Fig. 9c), and the data for this case is shown in Fig. 9a). The signals have been band-pass filtered to include only content with 5kHz<f<20 kHz. An inversion layer in the USXR emission is observable across chord 9; this chord is approximately tangent to the q=2 surface radius, and indicates the presence of a magnetic island at this radius. There is also a strong inversion across the magnetic axis (chord 2), indicating the presence of an odd-n core localized mode.

We have been able to reproduce the most important features of this calculation using model eigenfuctions. The eigenfunction is composed of a 2/1 magnetic island coupled to a 1/1 core kink. The radial location of the island is determined by the radius of the q=2 surface, and the width is an adjustable parameter. The core 1/1 kink is determined by a shift of the inner surfaces, where the magnitude of the shift and its radial extent are free parameters.

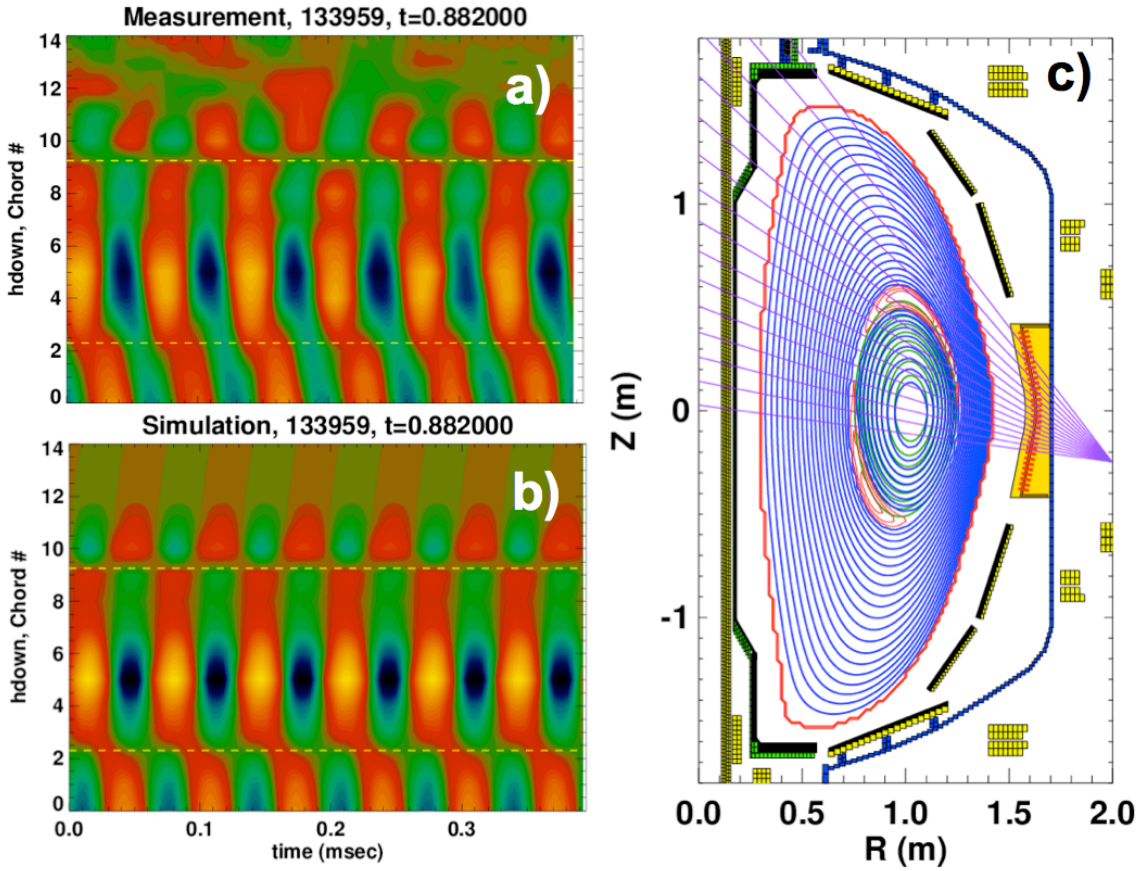

Fig. 9) Comparison of the a) measured and b) modeled USXR emission for the case with a strong core n=1 mode, and c) the model eigenfunction associated with the simulation. Chord #2 passes through the magnetic axis, while chord #9 is nearly tangent to the q=2 surface.

The free parameters are determined by the USXR data. The time- & chord-averaged emission is inverted to find $\varepsilon(\psi)$, the emission as a function of poloidal flux. Next, this emission is mapped to the eigenfunction. The emission is then integrated along the chords of the USXR array. This integration is then repeated for many phases of the island with respect to the detector array, mimicking the effect of plasma rotation on the detected signal. More information on this analysis process can be found in Appendix 1.

The result of such a simulation is shown in Fig. 9b), where the color scale, though arbitrary, is the same for both frames a) & b). The most prominent features of the measured contours are clearly reproduced. These include the inversion across chord 9, indicative of the m/n=2/1 island, and the inversion across the magnetic

axis, indicative of the 1/1 kink. Furthermore, the fluctuation amplitude is the same in both the measurement and simulations.

The eigenfunction from this calculation is shown in Fig. 9c), where the blue curves are the closed flux surfaces of the new perturbed equilibrium with the island and core kink. The magnetic islands are displayed in red. Also shown in green are the unperturbed magnetic surfaces inside the radius of the q=2 surface. The displacement between the blue and green surfaces in the plasma core provides a sense of the amplitude of the displacement; the present simulation indicates a displacement of ~2.5 cm is present for the core mode, and that the island width at the outboard midplane is ~6-7 cm.

Comparison of the simulated and measured emission contours in Fig. 9a) and b) also reveals the limitations of the present model. Most strikingly, the data in frame a) reveals that there may be an additional inversion layer outside the radius of the q=2 island. This is likely an m/n =3/1 magnetic island. Also, the somewhat different structure of the emission contours near the magnetic axis indicates that the simple m/n=1/1 kink model may be insufficient to capture all the details of the actual mode.

We have again used the neutron emission to find fast ion diffusivity profiles consistent with the data. As before, the D_{FI} profile was specified using eqn. 3 as a tanh profile of various widths and amplitude. All parameters were fixed in time for a given TRANSP calculation, but scanned in a series of independent TRANSP runs. Fig. 10a) shows that for zero anomalous diffusivity (the far left of the graph), the neutron emission is overestimated in TRANSP by a factor of ~30%. Shown in red are the simulated neutron rates for a very narrow profile of the diffusivity (w=0.15), where it is essentially impossible to match the measured emission except at very large diffusivity. However, for D_{FI} profile widths of w=0.3,0.45, and 0.6, it is possible to match the neutron emission using different values of the diffusivity magnitude. The D_{FI} profiles that allow a neutron rate match are shown in Fig. 10b), where it is clear that it is possible to trade off profile width and amplitude in order to match the neutrons. Resulting neutral beam current drive profiles are shown in Fig. 10c). It is clear that all three current drive profiles with $D_{FI}>0$ dramatically reduce the core

beam current drive, but also that the three beam current drive profiles are largely indistinguishable from each other.

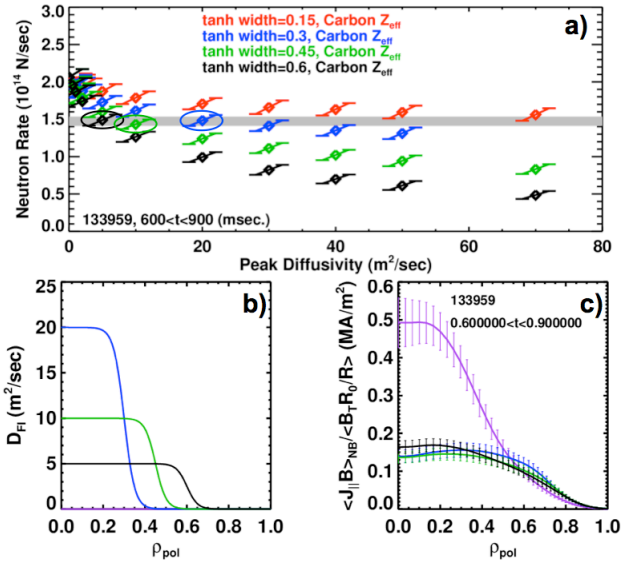

Fig. 10) Study for the determination of the fast ion diffusivity width and amplitude, for the discharge with coupled core 1/1+2/1 modes. Shown in a) are the measured neutron rate in gray, and the simulated neutron rate for a variety of diffusivity profiles and widths; the x-axis corresponds to the parameter A_{FI} in eqn. 3. Also shown are b) the diffusivity $D_{FI}(\rho_{pol})$ and c) the neutral beam current drive profiles, for a case without any anomalous diffusion (in purple), and three cases with diffusion to match the measured neutron rate. These three cases are circled in frame a).

Finally, the calculation of the current profile components is shown in Fig. 11a), where the color scheme is the same as used in Fig. 8. As with the previous case, the purely classical accounting for the current profile predicts excessive current near the magnetic axis, again due to the strong peaking of the neutral beam current. However, Fig. 11b) shows that using the TRANSP run with a D_{FI} profile width of 0.45 and a diffusivity of 10 m^2/sec (these are the parameters of the green curves in Fig. 10 b) and c)), the current profile accounting is much more accurate. Some discrepancy remains at r/a=0.5; this is potentially due to the errors in the n=0 profiles and equilibrium constraints due to the large rotating n=1 perturbations. In this case, the various current fractions are $f_{Ind}\approx$ 36%, $f_{PD}\approx$ 39%, and $f_{NB}\approx$17 %. These sum to 92%, implying that the sum over independently calculated current sources does not totally add up to the known toroidal current. As is discussed in Sect. 8, one

source of error is the somewhat lower current density at the plasma edge in the green curve, compared to the reconstruction in black.

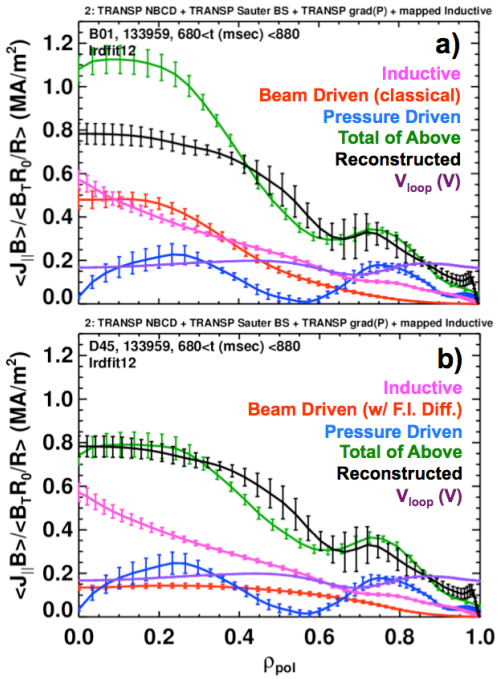

Fig. 11) Calculation of the current profile for discharge 133959, a) using classical beam slowing down, and b) including anomalous fast ion radial diffusion.

There have been a number of studies of core n=1 kink and tearing modes in NSTX H-mode plasmas. The first large study of n=1 core kink modes was published in Ref. [103]. It was shown there that these modes can cause severe rotation damping and degrade fast ion confinement. These studies were extended to understand the effect of the modes on the current profile in Refs. [67,68]. That reference illustrated that these core m/n=1/1 modes can cause significant fast ion current redistribution. A study of the neoclassical aspects of m/n=2/1 islands in NSTX was published in Ref. [104], demonstrating that multiple mechanisms can trigger these modes; cases were illustrated with energetic particle mode (EPM) triggers, ELM triggers, and "triggerless" mode strikes. It was also shown that the rotation shear at the q=2 magnetic surface was an important variable for determining the threshold neoclassical drive for striking the modes, a result also

found in DIII-D [105-107]. Saturated core n=1 modes have also been observed in MAST [108].

Reference [104] also described, but did not show in a figure, that the 2/1 modes are typically coupled to 1/1 core modes. This result is actually not uncommon, as the coupling of m/n neoclassical tearing modes to m-1/n core kinks has been documented in TFTR [109] and ASDEX –Upgrade [110] and predicted by theory [111]. Indeed, the destabilization of the 2/1 mode without an obvious trigger in Ref. [104] may be due to the m/n=1/1 mode providing the initial instability drive. The conditions under which either the 2/1 or 1/1 component dominates the triggering and saturation process in NSTX is not fully understood, and is the subject of continued study.

With respect to the redistribution of the neutral beam current, it is likely that both the central 1/1 mode and the higher-m islands play an important role. In general, it has been found that quasi-static magnetic perturbations produce islands in the phase-space trajectories of energetic ions [112]. A single magnetic perturbation can cause multiple phase space islands due to the coupling between then m=1 structure of the magnetic drifts and the magnetic perturbation. These drift islands themselves can enhance the fast ion transport; however, when they overlap, the transport is greatly increased. This overlap condition then sets the threshold for stochastic fast ion transport. If multiple-helicity magnetic perturbations are present, the threshold magnetic perturbation for stochastic transport can be reduced [112]. This explanation has been successfully applied to model fast ion loss due to low-frequency MHD in DIII-D [42], TFTR [113], and ASDEX-Upgrade [60-62,114]. The large mode amplitudes and multiple-harmonics in the present discharge make this explanation quite plausible for the present case. The detailed interaction of the fast ions with the complex magnetic perturbation is, however, out of scope for the present paper, and is a topic for future study.

Section 4.3: Discharge Free of Low Frequency MHD

The final discharge in the 0.7 MA, 0.48 T study, shot 133964, had a long MHD-free period. This achieved the lowest ever flat-top average loop voltage (130 mV) for a long-pulse NSTX H-mode discharge. The magnetic field pitch angle evolution for this discharge is shown in Fig. 12a), and illustrates that a nearly fully evolved current profile is achieved by the end of the discharge. The gray area in this figure indicates the time during which the current profile analysis is executed.

The current profile analysis is shown in Fig. 12b). The current profile accounting works quite well with no anomalous diffusion. The only large discrepancy occurs near the plasma edge, a common feature in this analysis that will be discussed in section 8. Note that the loop voltage profile is quite flat, indicating that any further evolution of the current profile is quite small. The total non-inductive fraction is 62-68% in the discharge, with f_{Ind}≈33%, f_{PD}≈49%, and f_{NB}≈14 %.

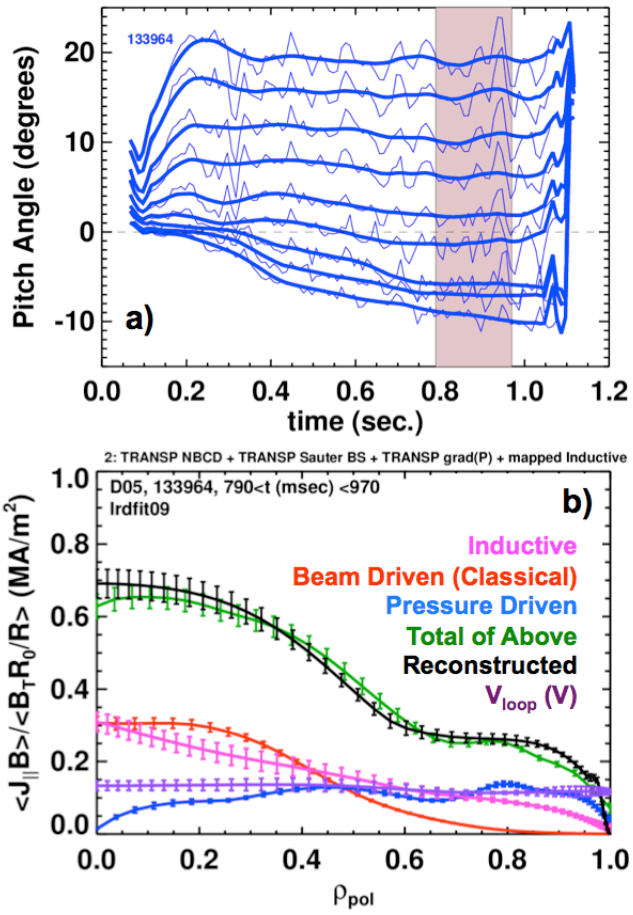

Fig. 12) Pitch angles (a) and current profile accounting (b) for the blue discharge in Fig. 4. The direct pitch angle data, in thin lines, has been smoothed

with a 100 msec time constant to produce the thick lines, in order to emphasize the slower evolution. This discharge achieved the lowest ever flat-top average loop voltage for a beam heated H-mode discharge.

We have also used this discharge to compute the expected q_0 evolution by solving the poloidal field diffusion equation in TRANSP using the measured plasma profiles and reconstructed boundary shape. The poloidal field diffusion solver was turned on at t=0.4 seconds, after most of the early MHD activity had subsided, and no anomalous diffusion of the beam particles is included in the simulation. The result of this calculation is shown in Fig 13. Considering the equilibrated state toward the end of the discharge, the value of q_0 calculated by TRANSP is within 0.1 units of that derived from MSE-constrained equilibrium reconstructions. This calculation shows again that the neoclassical calculation of the current profile agrees reasonably well with the reconstruction. It should be noted, however, that this does not validate use of the TRANSP poloidal field diffusion solver with purely neoclassical physics for all time-dependent simulations. In particular, Alfvenic and tearing activity during and just after the current ramp-up is quite common. Given the results of this section, it appears that this mode activity will almost surely modify the current profile evolution.

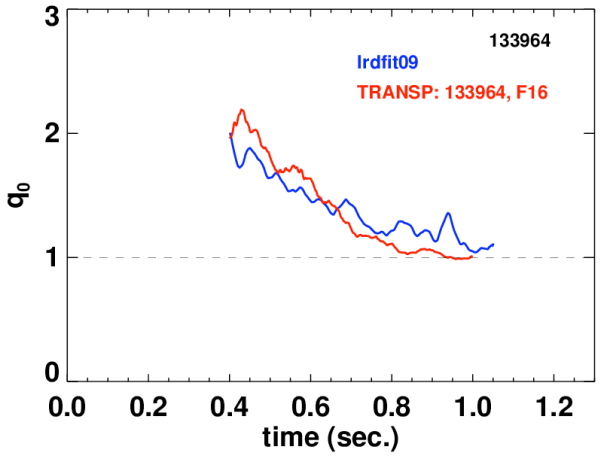

Fig 13) Comparison of the q_0 evolution from MSE constrained reconstructions (blue), and from a poloidal field diffusion calculation using TRANSP (red).

5: Current Profile Reconstructions in moderate-q_{95} Plasmas Optimized for Long Pulse

The second class of discharges selected for study were optimized for long-pulse operations. This requires that the magnitude of the toroidal field be reduced so that the coil heating limit is reached later in the discharge. The task is then to optimize the discharge parameters such that the current limit on the solenoid and heating limit on the toriodal field coil are reached simultaneously. The cases described here meet this criterion with I_P=0.7 MA and B_T=0.37 T, with q_{95}=11. We also note that a discharge subject to a similar optimization, and which lasted ~300 msec longer than those described here, was reported in Ref. [78].

Two example discharges from this set are shown in Fig. 14. The plasma current is displayed in frame a); these discharges have pulse lengths in excess of 1.5 seconds. The β_N evolution is shown in frame b), with values of ~5 common in these cases. Note the transient reduction in β_N at approximately 0.9 seconds in the blue trace, (discharge 135440), apparently due to a very large edge localized mode (ELM); as will be seen below, this transient leads to transition in the profiles, and development of a more quiescent plasma configuration. The reconstructed central safety factor is shown in frame c), and saturates above unity for both discharges in this study, indicating that the current profiles have stopped evolving. The solenoid current is shown in frame d). The two discharges have very similar flux consumption until the event in 135440; that discharge then uses flux at a somewhat lower rate. The current in a representative RWM coil is shown in frame e). The fluctuations in this signal are due to the n=1 mode feedback system [80,81], and the reduction in the fluctuation amplitude after t=0.8 sec. in 135440 is further indicative of the transition to the quiescent regime.

This interesting quiescent regime has additional desirable features. The volume integrated radiated power is shown in frame f). The discharge without the quiescent transition shows a continuous ramp of the radiated power, as is typical of discharges with lithium conditioning. However, the radiated power rise is arrested after the quiescent-regime transition in 135440. The density rise in frame g) is also stopped. This discharge has thus stopped evolving in both the current and the

kinetic profiles. No large rotating MHD activity (frame h)) is visible once the transient modes at the beginning of the discharge die away.

That these discharges reach a fully evolved current profile is illustrated not only by the q_0 evolution in Fig 14c), but also in the magnetic field pitch angle evolution shown in Fig 15). The traces shown are for discharge 135440 in blue above, which has the MHD event/ELM at t~0.9 sec. followed by transition to the more quiescent state. Note that the pitch angles have largely stopped evolving by ~0.7 seconds. After the ELM at ~0.9 sec., the deviation in time of the pitch angles is much reduced, providing additional evidence of the quiescence of the new configuration; any further pitch angle evolution is arrested by ~1.25 seconds. The shaded areas in the figure indicate the times for subsequent kinetic and current profile analysis.

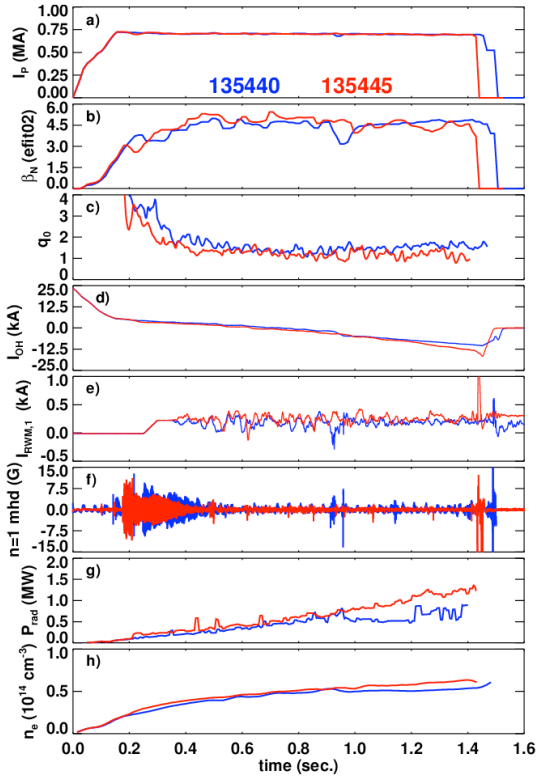

Fig 14) Time traces of two discharges designed to maximize the achievable pulse-length in NSTX. Shown are a) the plasma current, b) β_N, c) the safety factor on axis (q_0), d) the solenoid current, e) the current in a representative RWM coil, f) the n=1 rotating MHD signal, g) the radiated power, and h) the line-average density.

The kinetic profiles for discharge 135440 are shown in Fig. 16. The blue traces show the profiles before the ELM driving the transition to the new quiescent regime, while the black profiles are taken from after the transition. We see that, after that transition, the electron density decreases at the edge but increases in the core, while the deuterium density increases across the profile. This latter is the expected result when the impurities are flushed from the discharge, followed by a period without impurity accumulation. Note the local reduction of density gradient near ρ_{pol}=0.8 after the transition. This feature is also observed in the electron temperature after the transition, where the central electron temperature is slightly lower, but a larger drop occurs in the edge region ρ_{pol} >0.8.

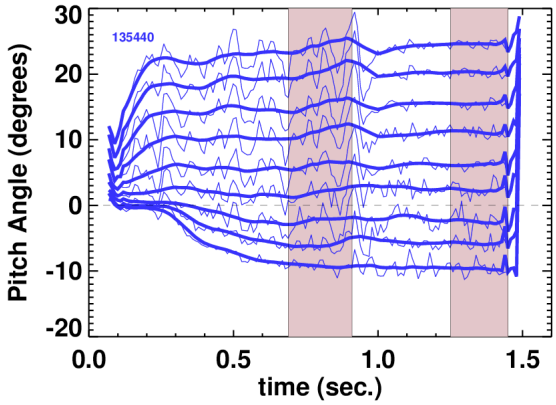

Fig. 15) Pitch angle evolution for shot 135440, the blue discharge in figure 14. The dark bands indicate the time windows for averaging in subsequent plots. Thin traces are the direct pitch angle data, while thick traces have a 100 msec smoothing filter applied in order to emphasize the slow evolution.

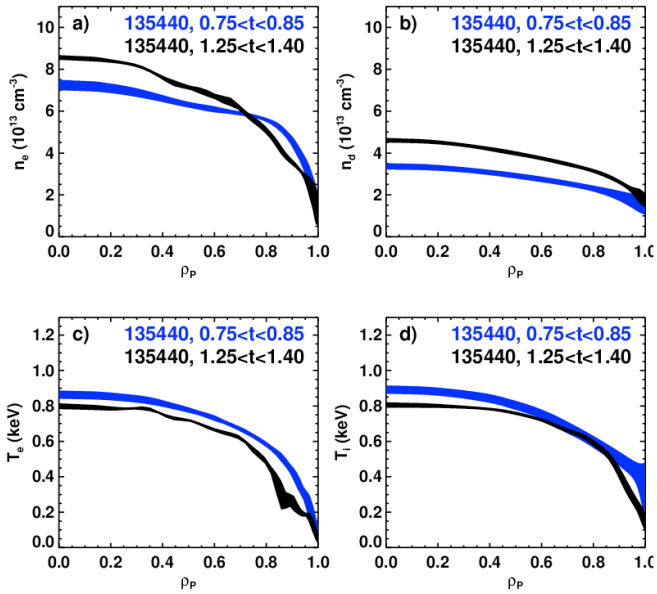

Fig. 16) Mapped kinetic profiles before and after the transition to the more quiescent conditions in discharge 135440. Shown are profiles of the a) the electron density profiles, b) the deuterium density, and c) the electron temperature, and d) the ion temperature.

We have applied these current profile reconstruction techniques to these discharges, and, as shown in Fig. 17, have found good agreement between the reconstructed current profile and that computed by summing the components. No fast ion diffusivity is used in these calculations. The current comparison before the confinement transition is shown in Fig. 17a), and looks quite similar to the higher q_{95} case in Fig. 12b). The current profile after the transition shows less current at the plasma edge, for both the reconstructed case and the constituent sum. This is due to the relaxation of the edge pressure gradient noted above, leading to a reduction of the bootstrap current in that region. In both cases, the loop-voltage profile is flat, again implying that the current profile has stopped evolving. The non-inductive fractions for the two time windows are f_{Ind}≈[41,37] %, f_{PD}≈[45,49] %, and f_{NB}≈[10,8] %, where the descrepencies with respect to 100% are mostly due to the inability of the constituent sum to perfectly match the reconstructed current density at the plasma edge.

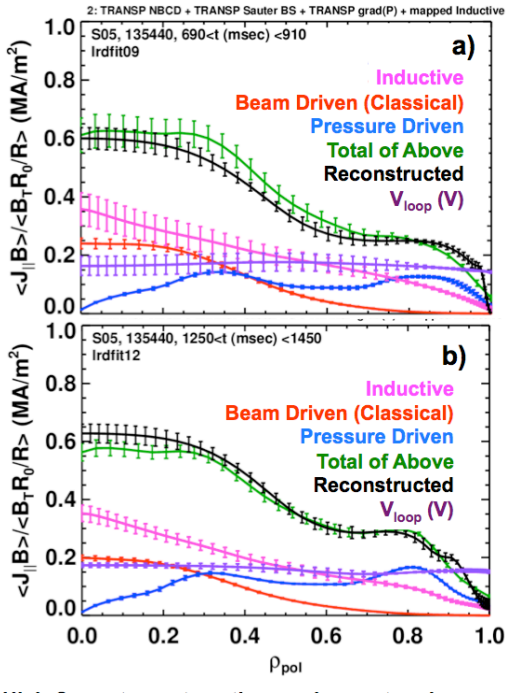

Fig. 17) Reconstruction of the current profile long-pulse discharge 135440. The profiles are for times a) before and b) after the change to the more quiescent configuration.

6: Current Profile Reconstructions in Low-q_{95} Plasmas Optimized for High Stored Energy and High β_T

The final set of discharges considered here are higher current cases, designed to maximize the sustainable toroidal beta or stored energy. These goals are typically met by increasing the plasma current and operating at reduced q_{95}. The maximum pulse duration is then determined by the flux consumption and solenoid current limit.

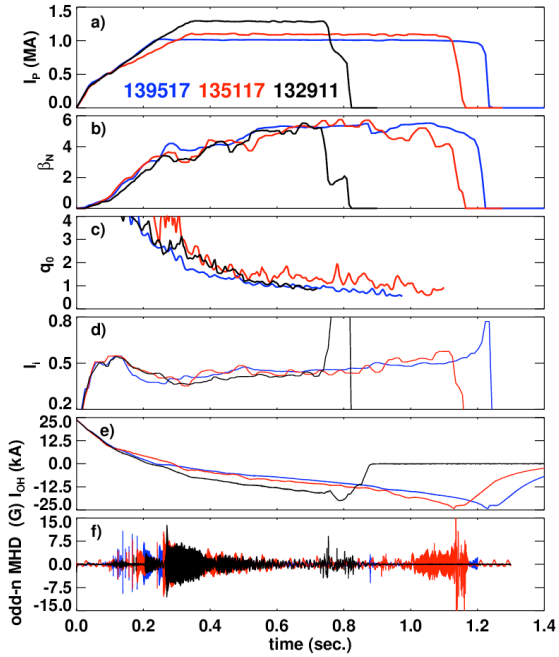

Fig. 18) Time traces of high-current discharges designed to maximize the stored energy (132911), and the sustainable value of β_t (135117 & 139517).

Time traces from example discharges are shown in Fig. 18. The plasma current from these three cases is shown in frame a), illustrating that these examples have 1 MA, 1.1 MA, and 1.3 MA of plasma current. The first two cases were run with a toroidal field of 0.45 T, while the 1.3 MA case was run with B_T=0.48 T. The β_N evolution in frame b) shows that all cases reach β_N in excess of 5. This corresponds to 430 kJ for the 1.3 MA plasma, which is close to the NSTX record of 460 kJ. The evolution of the central safety factor is shown in c), and it is clear that none of these cases have reached a stationary state by the end of the discharge. The internal inductance (l_i) is shown in frame d). This class of plasmas has among the lowest values of l_i in all beam heated discharges in NSTX, with β_N/l_i ratios up to 13.5 achieved. Indeed, the reduction in the I_P ramp rate in 135117 (the red discharge) was implemented in an attempt to avoid such low l_i levels. The solenoid flux is shown in frame e), and the odd-n low frequency MHD in frame f). The 1.1 MA case in red develops a rotating n=1 MHD mode at t=0.95, after which the slope of the solenoid current increases to a high rate to provide additional loop voltage.

Otherwise, the flux consumption essentially follows the plasma current level. Each discharge has a >100 msec period during which there is very little MHD activity. The calculations presented below for these discharges are done during this MHD-free window and do not use any anomalous fast ion diffusivity.

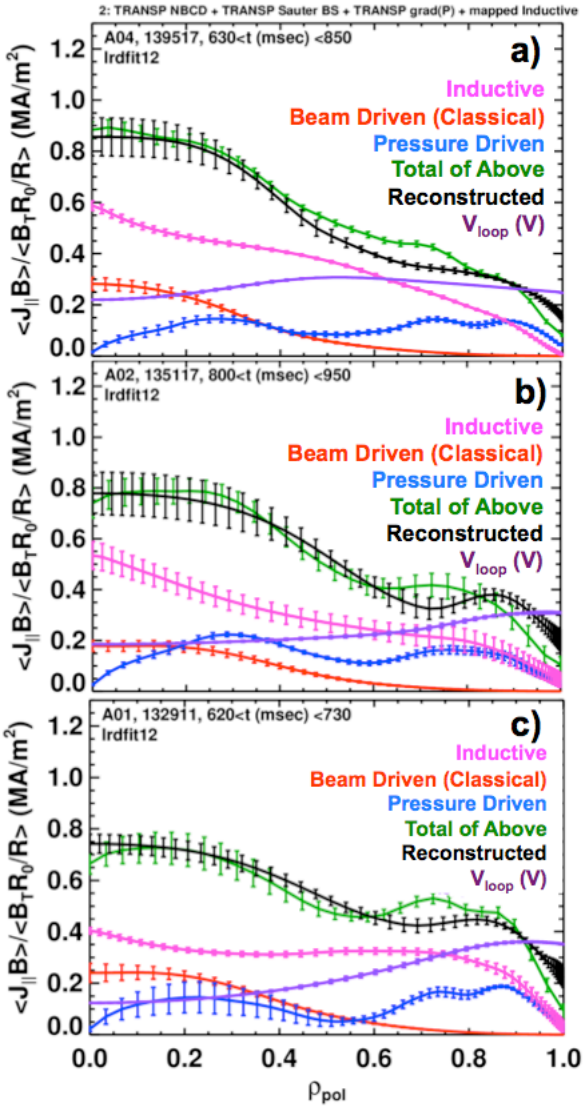

Fig. 19) Current profile reconstructions for the three discharges in Fig. 18. These cases have a) 1.0 MA at q_{95} of 8, b) 1.1 MA at q_{95} of 8, and c) 1.3 MA at q_{95} of 7.5

The current profile reconstruction for these three cases is shown in Fig. 19. We see that as before, the current profile accounting generally works well: the green and black curves are in reasonable agreement for all three cases. There are some

significant differences between these cases and those discussed previously. Most importantly, the loop voltage profiles for these cases are all hollow on average, indicating that the current profile has not yet come into equilibrium at these higher values of plasma current.

It was noted above that these plasmas tend to have lower values of the internal inductance l_i compared to those at lower current. This can be seen in the current profiles below, where, for instance, the current density at the top of the pedestal (ρ_{pol}~0.8) is a larger fraction of the central current density than for the lower current cases in Figs. 12b) and 17. Of course, these current profiles are not fully relaxed, and the central current would be larger once the loop voltage profiled flattened and the conductivity was allowed to determine the current density. These cases with plasma currents of [1.0, 1.1, 1.3] MA have current fractions of f_{Ind}≈[48,44,52] %, f_{PD}≈[38,38, 35] %, and f_{NB}≈[9,6,7]%, with the unaccounted for current occurring at the edge.

7. Upper Bounds of the Fast Ion Diffusivity in MHD-Free Discharges

As noted in Sect. 1, some previous studies of neutral beam current drive have invoked a small amount of anomalous fast ion diffusion, even in the absence of low-frequency MHD activity. In ASDEX-Upgrade experiments with off-axis NBCD, a diffusion coefficient of 0.5 m^2/s was used to enable the fast ion current to fill in on axis, yielding better agreement with the measured pitch angle evolution; this additional diffusivity was attributed to turbulent transport [60]. Experiments in DIII-D [48-50] found that the neutron emission, neutral beam current drive, and the FIDA spectrum are typically consistent with TRANSP calculations including classical processes only. The exception to this is the high injected power regime with small E/T (where E is the injected fast ion energy and T is the plasma temperature), where an anomalous fast ion diffusivity was also invoked; a threshold depending on E/T is consistent with some expectations from electrostatic turbulence [115,116]. Note that with injected ions in the 70-90 kV range and temperatures of ~1 keV in

neutral beam heated discharges, the E/T values in NSTX are much higher than the threshold values in the DIII-D studies.

The calculations presented in sections 3-6 show that in the absence of low-frequency MHD, NSTX results can be understood without invoking additional anomalous fast ion diffusion. However, this observation does not eliminate the possibility that some small level of anomalous fast ion diffusion may be present, and it is interesting to study whether the data can provide an upper bound on D_{FI} in these MHD-free discharges.

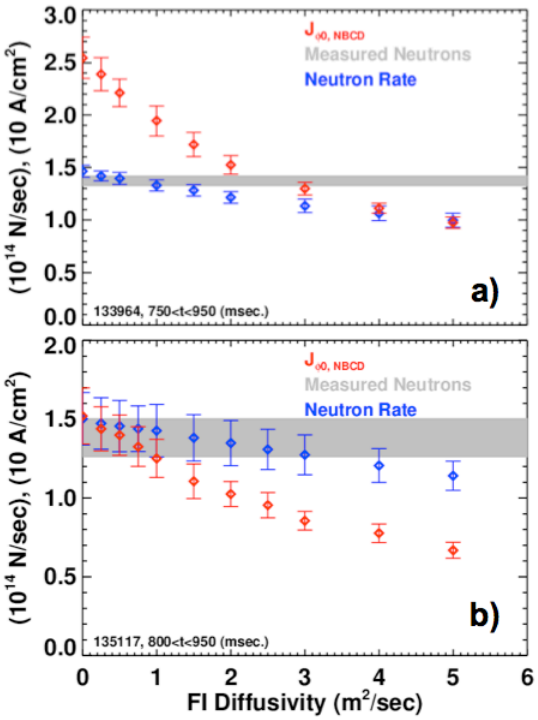

Fig. 20) The predicted neutron rate and central neutral beam toroidal current density, as a function of the imposed fast ion diffusivity. The gray line indicates the measured neutron emission rate, including the statistical variation of the signal within the averaging window. The shots shown are a) a 0.7 MA high-β_P shot (133964) and b) a 1.1 MA high-β_T discharge (135117).

We begin to assess this question by looking at simulations of high-q_{95}, high-β_P discharge 133964, studied in figure 12), and high-β_T discharge 135117, shown in figure 19b). We have run the TRANSP+NUBEAM code with various levels of fast ion diffusion, leaving all other input options fixed. The diffusion in this case is a constant in both space and time. Considering the neutron emission in Fig. 20, it appears that

fast-ion diffusivities in the range of $0<D_{FI}$ (m^2/s) <2 are essentially consistent with the measurement for 133964 in frame a), and up to 4 m^2/s for 135117 in frame b). The on-axis current density is more sensitive than the neutrons to the diffusivity, with D_{FI}=1 m^2/sec resulting in a ~20% reduction in the current density for both cases. This is essentially the highest value of D_{FI} (and current density reduction) consistent with the profiles in Figs. 12 and 19b).

Using the neutron rate to bound the possible fast ion diffusivity is subject to error if the absolute calibration on the detector is erroneous. The time-scale analysis described in section 3 can be used to eliminate uncertainties in this regard, as shown in Fig. 21. Frame a) shows the simulated decay time (τ_D) of the neutron emission as a function of fast ion diffusivity, while frame b) shows the rise time (τ_R), for the same discharges as were studied in Fig. 2. D_{FI} is a constant in both space and time for these simulations. As with the neutron emission rate itself, the simulated decay time is largely insensitive to values of $0<D_{FI}$ (m^2/s) <0.5. However, larger values of fast ion diffusivity, say, >2 m^2/sec appear to be excluded by this analysis.

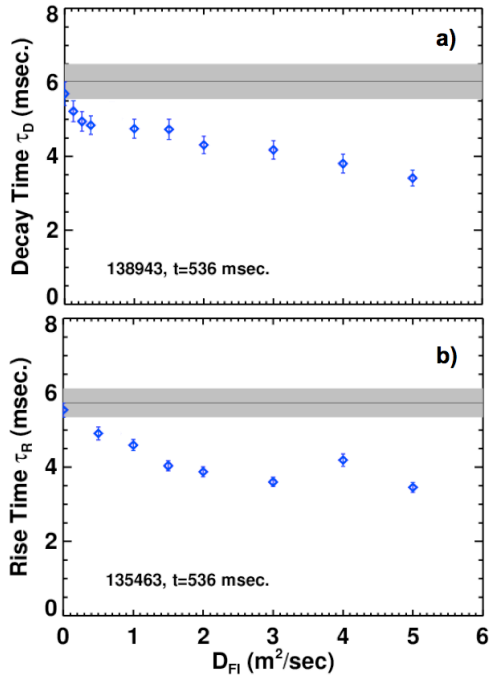

Fig. 21) Calculation of the a) rise and b) decay time constants, as a function of the applied fast ion diffusivity, for the two discharges shown in Fig 3. Diffusivities up to D_{FI}~0.5 m^2/sec are difficult to exclude based on this data.

Beyond the possibility for turbulent diffusion of fast ions noted above, high frequency Alfvenic activity in NSTX [97,117-119] could also provide a mechanism for the transport of fast ions, in either physical or velocity space. An example of this activity is shown in Fig. 22, where the spectrogram for the high-β_P shot 133964 is shown; the neoclassical accounting of the current profile in Fig. 12 worked out cleanly in this case. While, as noted above, there is no low-frequency MHD activity, there remains considerable high-frequency activity. These modes have been identified as global and compressional Alfven eigenmodes (GAEs and CAEs). There is some evidence that these modes may contribute to electron transport in NSTX [120], and the suggestion that they may provide a mechanism for the fast-ions to directly heat thermal ions [121]. The study of these high-frequency CAE/GAE modes, and their impact on the global plasma performance, is an active part of the NSTX research program.

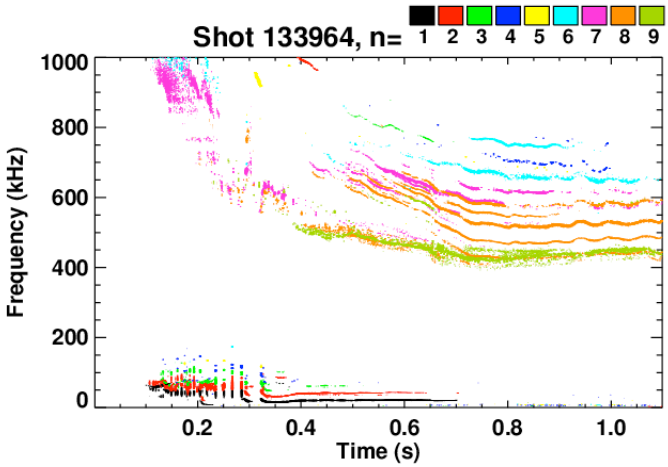

Fig. 22) Spectrograms of the MHD activity for high-β_P discharge 133964. Many high-frequency modes can be identified during the phase of the successful current profile analysis (800<t<1000 msec).

8. Discussion and Summary

This paper has presented a systematic analysis of the current profile in NSTX high-performance NB heated H-modes, with a goal of establishing when standard neoclassical calculations of the current profile are experimentally justified. For the conditions studied in this paper, we have found that:

- The neoclassical picture generally holds when low-frequency MHD is absent. This has been established over a range of q_{95} in high-elongation, high performance NB heated plasmas.
- The neoclassical calculation generally fails when low-frequency MHD modes are present. Examples given here include TAE avalanches, and large coupled m/n=1/1+2/1 modes. Agreement can generally be recovered in these cases when an anomalous fast ion diffusivity is invoked.
- There is an upper bound of ~1-2m^2/sec on the fast ion diffusivity in mhd-free discharges.

Neoclassical calculations of this sort are often used to predict the ramp-up characteristics and steady state current profile for the purpose of device design. The results in this paper are mildly encouraging, in that the stationary profile predictions using only neoclassical physics appears justified in the absence of low-frequency MHD.

However, as noted in Ref. [37] with respect to tearing modes, the assumption of neoclassical neutral beam current drive to ramp-up the plasma current may be questionable, given that these would likely be low(er) density plasmas with substantial fast ion beta, a condition that is conducive to fast-particle driven MHD. Indeed, the ramp-up phase of most NSTX H-mode discharges has considerable fast-particle MHD. The conclusive prediction of the onset regime for these modes, and the fast ion transport they cause, is a subject of continued research.

In addition to these observations regarding the current profile, a number of interesting plasma conditions have been observed. These include:

- Discharges that maintain 65-70% non-inductive fraction for many current redistribution times (τ_{CR}~300 msec), without strong MHD activity. These are an improvement on the discharge noted in Refs. [67,68], where the high non-inductive fraction phase is terminated by core n=1 modes.

- An interesting example where a modification to the plasma profiles after an MHD event leads to an improved "quiescent" configuration.
- Cases that have reached a fully evolved current profile.
- Use of USXR data to determine the structure of a coupled m/n=2/1 magnetic island and 1/1 core kink.

Section 7 showed that the NSTX data in MHD free cases is consistent with a small value of fast ion diffusivity. While these small values have a minimal effect on the beam current drive for the present discharges, devices configured for substantial off-axis current drive may be more heavily impacted (the actual effect of the turbulence or high-frequency MHD modes may not be strictly diffusive, but we treat it that way here for convenience). This is illustrated by an example calculation in Fig. 23, where the driven current profiles for a single 90 kV, 2 MW deuterium source are shown for three different tangency radii (R_{tan}) and five values of the spatially and temporally constant fast ion diffusivity. The target discharge is the 1.1 MA case shown in Fig. 19b), where the magnetic axis is at R_{maxis}=105 cm. The R_{tan}=70 cm case in frame a) is essentially similar to the present NSTX source A, with a broad driven current profile. Increasing the fast ion diffusivity to 0.5 m^2/sec causes a ~13% drop in the central beam current density. For the R_{tan}=100 cm calculation in b), the net current drive is significantly higher, and the effect of 0.5 m^2/sec is to reduce the beam current density by ~22%. Note, however, that as D_{FI} is increased, the total current remains unchanged, and the current density profile becomes broader, but without a profound change in radial structure.

The situation is qualitatively different for the R_{tan}=130 cm case. The driven current peak with D_{FI}=0 is located significantly off axis, resulting in a very hollow profile. The inclusion of D_{FI}=0.5 m^2/sec results in a 50% increase in the central current density, and a 25% decrease in the off-axis peak amplitude; the net effect is to fill in the hollow profile. The utility of the beam for q_{min} control would thus be partially compromised, though, for the flat D_{FI} profiles used here, the fast ion total current is not changed. Hence, further experiments to resolve small levels of anomalous fast ion transport are important. It is important to note that the details of

this calculation would change in response the changes in the plasma current magnitude and profile, changes in the kinetic profiles, or additional charge exchange loss. However, the spirit of the calculation, that off-axis current drive may be more sensitive to small amounts of fast ion diffusion, remains. Note that a similar conclusion was drawn for ASDEX-Upgrade in Ref. [60], and observed in references [47,48] and [65].

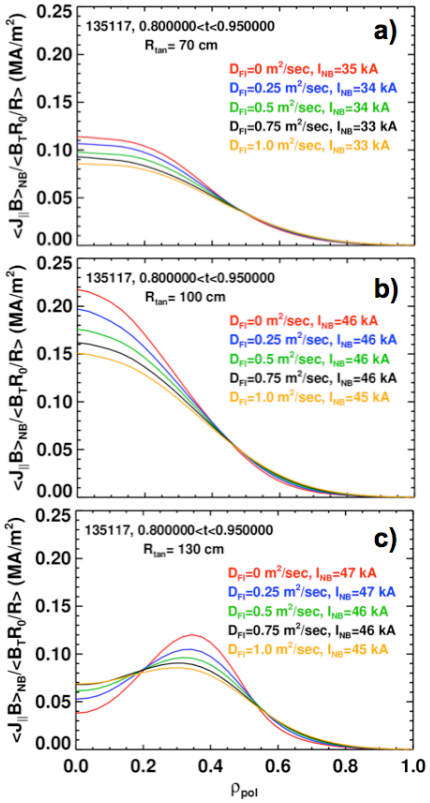

Fig. 23) Predicted neutral beam current drive profiles as a function of fast ion diffusivity, using the profiles from 1.1 MA ***shot 135117, for beam tangency radius of a) 70 cm, b) 100 cm, and c) 130 cm. The diffusivity is constant and space in time.***

With regard to prediction of the current profile for next step-devices, the fact remains that although anomalous fast ion diffusion may (or may not) be present, anomalous diffusion of thermal plasma particles, momentum, and heat remains an unsolved problem. In particular, the bootstrap current depends sensitively on the density and temperature gradients, which must be predicted based on models of the sources and sinks of particles and energy. Integrated modeling of conventional aspect ratio devices (see, for instance, Ref. [56] or [44]) have typically used reduced

transport models such as GLF23 [122]. However, it remains unclear that these models can accurately represent the transport in a spherical torus, and this remains an area of active research [123]. We also note that since the particle and energy transport can respond to changes in the current density and magnetic shear, it is ultimately necessary to solve for all profiles self-consistently.

It is also worth noting a few sources of systematic error in the calculations presented above. The largest discrepancy between the reconstructed and "summed" current profile is typically at the very edge of the plasma. Given that this region is heavily weighted in the area integral that determines the total current, a small error there can result in a large error in the total toroidal current. We have found that the reconstruction of the current profile in this region is quite sensitive to the basis functions used in the parameterization of $p'(\psi)$ and $ff'(\psi)$; it is desirable to provide sufficient freedom in the profiles to fit the data, consistent with time-slice to time-slice similarity of the reconstructions (in order to provide a smooth evolution of the poloidal flux for the loop voltage calculation) . The calculations here attempt to balance these constraints. We find, however, that our best effort reconstructions tend to produce larger current densities in that region than can be accounted for by summing the pressure-driven and inductive currents (the neutral beam driven current is predicted to be quite small at this radius). It is possible that a different parameterization of the edge profiles in the reconstruction code could help resolve this discrepancy. Alternatively, refined models of the bootstrap current, especially at the plasma edge, may be important.

A second systematic error could arise from centrifugal effects. The carbon density in NSTX is measured at the outboard midplane; it is then typically assumed that the densities measured there are indicative of all other points on the magnetic surface. However, centrifugal effects will lead the carbon to accumulate on the outboard midplane, causing this analysis to overestimate the global carbon density and inventory.

In order to correct for this effect, we have applied a centrifugal correction to the data, using methods described in Ref. [124] and previously applied to NSTX in

reference [101]. First, the outboard mid-plane (OMP) values of the carbon and electron density are computed as a function of poloidal flux. These densities, and deuterium from quasi-neutrality, are then mapped around the magnetic surface by iteratively solving the quasi-neutrality constraint and the expression for the poloidal distribution of density for a each species [124]:

$$n_j(\theta) = n_{j,OMP} \exp\left(\frac{\frac{1}{2} m_j \omega^2 \left(R(\theta) - R_0^2 \right) - eZ_j \varphi(\theta)}{T_j} \right) \qquad [4]$$

for all species; the outcome of the calculation is the poloidal electric field $\varphi(\theta)$. Here, θ is the poloidal angle, j is an index over the three species, and the iteration was started with eqn. 9 of [124]. Note also that the deuterium rotation frequency was taken to be equal to that for carbon; this could be resolved by taking the neoclassical deuterium toroidal rotation velocity from TRANSP, at the expense of increasing the complexity of the calculation. Once the deuterium, carbon, and electron densities are known as a function of poloidal angle on each magnetic surface, $Z_{eff}(\theta)$ can be computed. The flux-surface average can then be calculated, providing the radial profile of $\langle Z_{eff} \rangle$ for calculations of the current components.

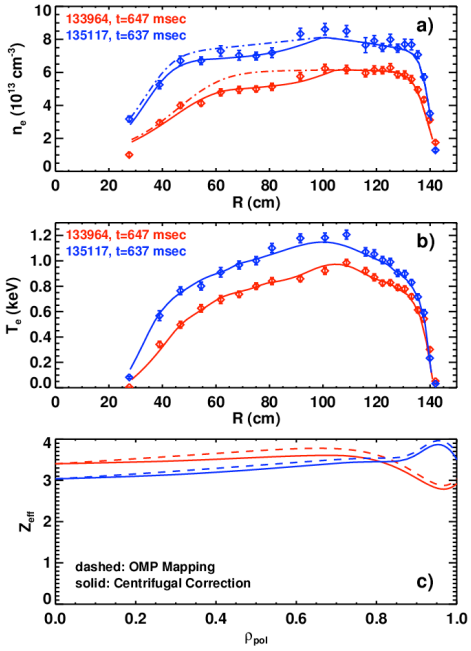

Fig. 24) Study of centrifugal effects on the Z_{eff} profile for two high-performance discharges. Shown are the a) electron density and b) temperature profiles vs. major radius across the midplane, and the c) mapped Z_{eff} profiles.

An example of these calculations is shown in Fig. 24, for time slices from the high-β_P shot 133964 (Fig. 12) and high-β_T shot 135117 (Fig. 19b)). Frame a) shows the measured density profiles across the midplane. The dashed line shows a fit where only the data on the OMP was used as a constraint. The fit matches well on the outboard side, but clearly overestimates the data on the inboard side. The solid lines show the midplane electron density from the iterative solution of eqn. [4], where a significantly improved fit to both sides of the profile is achieved. For reference, the electron temperature profiles are shown in frame b), where the fit is derived from both the inboard and outboard sides; no significant inboard/outboard error is seen, as expected given the high parallel thermal conductivity.

The Z_{eff} profiles for these two cases are shown in frame c), where the dashed line uses simple outboard midplane mappings, and the solid line uses the flux-surface average of the poloidally mapped species densities. The calculation with centrifugal corrections shows a slight reduction in Z_{eff}. Inclusion of the effect in calculations of the total inductive current typically yields a ~10 kA increase, which is ~1% of the total current. This explains a small amount of the discrepancy in the total current accounting noted in multiple places above. Given the marginal benefit and additional complexity of this centrifugal correction, we have not applied it to the calculations presented in Sections 3-6. The calculation does show, however, that centrifugal effects continue to be important in determining the profile shapes in these high-performance plasmas.

In summary, the results presented in this paper demonstrate that, in the absence of low frequency MHD activity, the current profile in NSTX high-β plasmas can be understood using (neo)classical physics only. This result holds over a range of q_{95}. However, when low-frequency MHD is present, the addition of some anomalous diffusion of the beam ions is required. The results do not, however, exclude the possibility of some small level of fast ion diffusivity (D_{FI}<~0.5-2 m^2/sec.)

in discharge free of low-frequency MHD. Diffusivities at this level or smaller could have a significant effect on the current drive localization for off-axis neutral beams. The proposed NSTX-Upgrade [125] could provide important additional information on this topic by providing six total NB sources with tangency radii from 50 to 130 cm, enabling off-axis NBCD studies in full-sized, high-β ST plasmas.

Acknowledgements

The authors wish to acknowledge Dennis Mueller, Roger Raman, and Tim Stevenson for their skilled operation of NSTX during these experiments, and thank Bill Heidbrink for his useful comments. This research was funded by United States Department of Energy Contract D-AC02-09CH11466

References:

[1] Y.K.M. Peng and D.J. Strickler, Nuclear Fusion **26**, 769 (1986) .

[2] R.J. Goldston, et al., *An Experiment to Tame the Plasma Material Interface*, in Fusion Energy 2008 (Proc. 22nd Int. Conf. Geneva, 2008) (Vienna: IAEA) CD-ROM file FT/P3-12 and http://www-naweb.iaea.org/napc/physics/FEC/FEC2008/html/index.htm

[3] M. Abdou, Fusion Eng. And Design **27**, 111 (1995).

[4] H.R Wilson, et al., *A Steady State Spherical Tokamak for Components Testing*, in Fusion Energy 2004 (Proc. 20th Int. Conf. Vilamoura, 2004) (Vienna: IAEA) CD-ROM file FT/3-1Ra and http://www-naweb.iaea.org/napc/physics/fec/fec2004/datasets/index.html

[5] Y-K M Peng, et al., Plasma Phys. Control. Fusion **47**, B263 (2005).

[6] G. M. Voss, et al., Fusion Eng. and Design **83**, 1648 (1648).

[7] Y.K.M. Peng, et al., *Extensive remote handling and conservative plasma conditions to enable fusion nuclear science R&D using a component testing facility*, in Fusion Energy 2008 (Proc. 22nd Int. Conf. Geneva, 2008) (Vienna: IAEA) CD-ROM file FT/P3-14 and http://www-naweb.iaea.org/napc/physics/FEC/FEC2008/html/index.htm

[8] F. Najmabadi and the ARIES Team, Fusion Eng. And Design **65**, 2003 (143).

[9] S. C. Jardin, et al., Fusion Eng. And Design **65**, 165 (2003).

[10] A. Sykes, et al., Nuclear Fusion **32**, 694 (1992).

[11] M. Gryaznevich, et al., Phys. Rev. Lett. **80**, 3972 (1998)

[12] D. A. Gates, et al., Phys. Plasmas **5**, 1775 (1998).

[13] R.J. Akers, et al., Nuclear Fusion **42**, 122 (2002).

[14] R.L. Miller, et al., Phys. Plasmas **4**, 1062 (1997).

[15] J.E. Menard, et al., Nuclear Fusion **37**, 595 (1997).

[16] R.J. Bickerton, J.W. Connor, and J.B. Taylor, Nature (London), Phy. Sci. **229**, 110 (1971).

[17] A. A. Galeev, Sov. Phys. JETP **32**, 752 (1971).

[18] M. C. Zarnstorff and S. C. Prager, Phys. Rev. Lett. **53**, 454 (1984).

[19] C.E. Kessel, Nuclear Fusion **34**, 1221 (1994).

[20] A.G. Peeters, Plasma Phys. Control. Fusion **42**, B231 (2000).

[21] M. Ono, et al., Nuclear Fusion **40**, 557 (2000).

[22] A. Sykes et al., Nuclear Fusion **41**, 11 (2001).

[23] C.B. Forrest, et al., Phys. Rev. Lett., **73**, 2444 (1994).

[24] O. Sauter, C. Angioni, and Y.R. Lin-Liu, Phys. Plasmas **6**, 2834 (1999).

[25] S. P. Hirshman, Phys. Fluids **31**, 3150 (1988).

[26] W. A. Houlberg, et al., Phys. Plasmas **4**, 3230 (1997).

[27] T. Ohkawa, Nuclear Fusion **10**, 185 (1970).

[28] D. F. Start, et al., Phys. Rev. Lett. **40**, 1497 (1978).

[29] D.F.H. Start and J.G. Cordey, Phys. Fluids **23**, 1477 (1980).

[30] D.F.H. Start, J.G. Cordey, and E.M. Jones, Plasma Physics **22**, 303 (1980).

[31] N.J. Fisch, Rev. Modern Physics **59**, 175 (1987).

[32] W.W. Heidbrink and G.J. Sadler, Nuclear Fusion **34**, 535 (1994).

[33] Y.R. Lin-Liu and F.L. Hinton, Phys. Plasmas **4**, 4179 (1997)

[34] R. J. Goldston, et al., J. Comp. Phys. **43**, 61 (1981).

[35] A. Pankin, et al., Comput. Phys. Commun. **159**, 157 (2004).

[36] P.A. Politzer, Phys. Plasmas **1**, 1545 (1994).

[37] C.B. Forest, et al., Phys. Rev. Lett. **79**, 427 (1997).

[38] T.C. Luce, Plasma. Phys. Control. Fusion **41**, B119 (1999).

[39] C. C. Petty et al., Nuclear Fusion **39**, 1421 (1999).

[40] C. C. Petty, Plasma Phys. Control. Fusion **42**, B75 (2000).

[41] M.R. Wade, et al., Phys. Plasmas **8**, 2208 (2001).

[42] E.M. Carolipio, et al., Nuclear Fusion **42**, 853 (2002).

[43] C. M. Greenfield, et al., Phys. Plasmas **11**, 2616 (2004).

[44] M. Murakami, et al., Nuclear Fusion **45**, 1419 (2005).

[45] T.C. Luce for the DIII-D Team, Nuclear Fusion **45**, S86 (2005).

[46] E.J. Doyle, et al., Plasma Phys. Control. Fusion **48**, B39 (2006).

[47] M. Murakami, et al., Nuclear Fusion **49**, 065031 (2009).

[48] J.M. Park, et al., Phys. Plasmas **16**, 092508 (2009).

[49] W.W. Heidbrink, et al., Phys. Rev. Lett. **103**, 175001 (2009).

[50] W.W. Heidbrink, et al., Plasma Phys. Control. Fusion **51**, 125001 (2009).

[51] C. T. Holcomb et al., Phys. Plasmas **16**, 056116 (2009).

[52] C.D. Challis, et al., Nuclear. Fusion **29**, 563 (1989).

[53] E. Joffrin, et al., Nuclear Fusion **45**, 626 (2005).

[54] X. Litaudon, et al., Nuclear Fusion **47**, 1285 (2007).

[55] I.T. Chapman, et al., Plasma Phys. Control. Fusion **50**, 045006 (2008).

[56] I. Voitsekhovitch, et al., Nuclear Fusion **49**, 055026 (2009).

[57] T. Oikawa, et al., Nuclear Fusion **40**, 435 (2000).

[58] T. Suzuki, et al., Nuclear Fusion **48**, 045002 (2008).

[59] M.C. Zarnstorff, et al., Phys. Fluids B **2**, 1852 (1990).

[60] S. Günter, et al., Nuclear Fusion **47**, 920 (2007).

[61] M. Garcia-Munoz, et al., Nuclear Fusion **49**, 085014 (2009).

[62] M. Garcia-Munoz, et al., Nuclear Fusion **47**, L10 (2009).

[63] K.L. Wong, et al., Phys. Rev. Lett **93**, 085002 (2004).

[64] K. L. Wong, et al., Nuclear Fusion **45**, 30 (2005).

[65] M. Turnyanskiy, et al., Nuclear Fusion **49**, 065002 (2009).

[66] R. J. Hawryluk, et al., "An Empirical Approach to Tokamak Transport", in Physics of Plasmas Close to Thermonuclear Conditions, ed. by B. Coppi, et al., (CEC, Brussels, 1980), Vol. 1, pp. 19-46.

[67] J.E. Menard, et al., Phys. Rev. Lett **97**, 095002 (2006).

[68] J.E. Menard et al., Nuclear Fusion **47**, S645 (2007).

[69] D. A. Gates, et al., Nuclear Fusion **47**, 1376 (2007).

[70] S. M. Kaye, et al., Nuclear Fusion **45**, S168 (2005).

[71] M. G. Bell, et al., Nuclear Fusion **46**, S565 (2006).

[72] D. A. Gates, et al., Phys. Plasmas **13**, 056122 (2006).

[73] D. A. Gates, et al., Nuclear Fusion **49**, 104016 (2009).

[74] W.W. Heidbrink, et al., Nuclear Fusion **43**, 883 (2003).

[75] D.A. Gates, et al., Phys. Plasmas **10**, 1659 (2003).

[76] D.A. Gates, et al., Nuclear Fusion **46**, S22 (2006).

[77] D.A. Gates, et al., Nuclear Fusion **46**, 17 (2006).

[78] J.E. Menard, et al., Nuclear Fusion **50**, 045008 (2010).

[79] S.P. Gerhardt, et al., Plasma Phys. Control. Fusion **52**, 104003 (2010).

[80] S.A. Sabbagh, et al., Phys. Rev. Lett. **97**, 045004 (2006).

[81] S.A Sabbagh, et al., Nuclear Fusion **50**, 025020 (2010).

[82] S.P. Gerhardt, et al., *Performance of Discharges with High Elongation and Beta in NSTX and Near-Term Paths Toward Steady State*, IAEA Fusion Energy Conference, Paper EXS/P2-08, Seoul (2010).

[83] H.W. Kugel, et al., Phys. Plasmas **15**, 056118 (2008).

[84] M. Bell et al., Plasma Phys Control Fusion **51**, 124054 (2009).

[85] R. Maingi, et al., Phys. Rev. Lett. **103**, 075001 (2009).

[86] S. Ding, et al., Plasma Phys. Control. Fusion **52**, 015001 (2010).

[87] R. Maingi, et al., Nuclear Fusion **50**, 064010 (2010).

[88] B.P. LeBlanc, et al., Rev. Sci. Instrum. **74**, 1659 (2003).

[89] F. Levinton and H. Yuh, Rev. Sci. Instrum. **79**, 10F522 (2008).

[90] http://w3.pppl.gov/~jmenard/software/lrdfit/lrdfit-index.htm

[91] O. Sauter, C. Angioni, and Y.R. Lin-Liu, Phys. Plasmas **9**, 5140 (2002).

[92] W. W. Heidbrink, et al., Phys. Fluids B **3**, 3167 (1991).

[93] T. Suzuki, et al., *Experimental Investigation And Validation of Neutral Beam Current Drive for ITER through ITPA Joint Experiments*, IAEA Fusion Energy Conference, Paper ITR/P1-14, Seoul (2010).

[94] M. Podesta, et al., Phys. Plasmas **16**, 056104 (2009).

[95] A. Bortolon, et al., Rev. Sci. Instrum **81**, 10D728 (2010).

[96] E. D. Fredrickson, et al., Phys. Plasmas **16**, 122505 (2009).

[97] E.D. Fredrickson, et al., Phys. Plasmas **13**, 056109 (2006).

[98] C. Z. Cheng, Phys. Rep. **211**, 1 (1992).

[99] N. N. Gorelenkov, C.Z. Cheng, and G.Y. Fu, Phys. Plasmas **2**, 2802 (1999).

[100] R.B. White and M.S. Chance, Phys. Fluids **27**, 2455 (1984).

[101] D.R. Smith, et al., Rev. Sci. Instrum. **81**, 10D717 (2010).

[102] D. Stutman, et al., Rev. Sci. Instrum. **70**, 572 (1999).

[103] J.E. Menard, et al., Nuclear Fusion **45**, 539 (2005).

[104] S.P. Gerhardt, et al., Nuclear Fusion **49**, 025005 (2009).

[105] R. J. Buttery, et al., Phys. Plasmas **15**, 056115 (2008).

[106] R. J. La Haye and R. J. Buttery, Phys. Plasmas **16**, 022107 (2009).

[107] R.J. La Haye, et al., Phys. Plasmas **17**, 056110 (2010).

[108] I.T. Chapman, et al., Nuclear Fusion **50**, 045007 (2010).

[109] E. D. Fredrickson, Phys. Plasmas **9**, 548 (2002).

[110] J.P. Meskat, et al., Plasma Phys. Control. Fusion **43**, 1325 (2001).

[111] D. Brennan, et al., Phys. Plasmas **14**, 056108 (2007).

[112] H.E. Mynick Phys. Fluids B **5**, 1476 (1993).

[113] S. J. Zweben, et al., Nuclear Fusion **39**, 1097 (1999).

[114] M. Gobbin, et al., Nuclear Fusion **49,** 095021 (2009).

[115] W. Zhang, et al., Phys. Rev. Lett **101**, 095001 (2008).

[116] T. Hauff, et al., Phys. Rev. Lett. **102**, 075004 (2009).

[117] N.N. Gorelenkov, et al., Phys. Plasmas **11**, 2586 (2004).

[118] E.D. Fredrickson, et al., Phys. Plasmas **11**, 3563 (2004).

[119] E.D. Fredrickson, et al., Nuclear Fusion **46**, S926 (2006).

[120] D. Stutman, et al., Phys. Rev. Lett **102**, 115002 (2009).

[121] D. A. Gates, et al., Phys. Rev. Lett. **88**, 205003 (2001).

[122] R. E. Waltz, et al., Phys. Plasmas **4**, 2482 (3230).

[123] G.M. Staebler, G. Colyer, S. Kaye, J.E. Kinsey, and R.E. Waltz, *Testing the Trapped Gyro-Landau Fluid Transport Model with Data from Tokamaks and Spherical Tori*, in Fusion Energy 2008 (Proc. 22nd Int. Conf. Geneva, 2008) (Vienna: IAEA) CD-ROM file TH/P8-42 and http://www.naweb.iaea.org/napc/physics/FEC/FEC2008/html/index.htm

[124] J.A. Wesson, Nuclear Fusion **37**, 577 (1997).

[125] J.E. Menard, et al., *Physics Design of NSTX Upgrade*, 37th European Physical Society Conference on Plasma Physics, Dublin, Ireland, online: http://ocs.ciemat.es/EPS2010PAP/pdf/P2.106.pdf

Appendix 1: Modeling of the USXR Emission from Coupled Kink-Tearing Modes.

The modeling of the USXR emission due to the coupled 2/1+1/1 modes requires two steps: i) calculation of the USXR emission, to calculate the emissivity as a function of minor radius (normalized poloidal flux), and iii) construction of a model eigenfuction for the MHD mode, and iii) mapping of the emissivity to the eigenfunction and integrating along the USXR detector lines of sight.

The USXR emission is calculated via an inversion of the chordal emission, averaged over many instances of the mode structure rotating in front of the detector array. A regularized inversion scheme is used, in order to find an emission profile that is radially smooth but consistent with the chordal emission. No attempt is made to compute the emission from a first principle emission calculation. The net result of this step is the emission as a function of normalized poloidal flux.

The mode eigenfunction in this calculation is composed of both a core m/n=1/1 kink and a 2/1 magnetic island. The 2/1 island is modeled via the method described in reference [103]: the helical flux is computed, a perturbation resonant with the 2/1 surface is imposed, and the island structure is computed. The radius of the island chain is determined by the location of the q=2 surface, and the width of the islands is set by adjusting the amplitude of the helical flux to match the observed USXR emission contours.

The m/n=1/1 perturbation is then added to the model. The displacement is modeled as a rigid perturbation to the helical flux function in the plasma core, whose radial structure is given by $\xi_{1,1} = \begin{cases} \xi_0, & r < r_c \\ \xi_0 e^{-\left[(r-r_c)/r_f\right]^2}, & r > r_c \end{cases}$. The parameters r_c, r_f, and ξ_0 determine the radial region of the perturbation, the radial fall-off width, and the size of the shift. The phase of the 1/1 perturbation is generally set so that the displacement is in the large major-radius direction at toroidal angles where one of the 2/1 mode X-points is on the outboard side. We note that this is not a theory based model for the 1/1 mode; the merit of this approach is that it allows easy comparison to the measurements.

The emission function previously calculated is then mapped onto the new equilibrium with the island/kink; the emission is assumed to be constant within the island. The emission is then integrated for along the line of sight of the USXR detectors, for different phases of the coupled 2/1+1/1 structure with respect to the toroidal angle of the USXR array, in order to simulate the effect of plasma rotation. For instance, the calculation in Fig. 9 used 24 toroidal phases between 0 and 2π to provide good resolution along the x-axis. A fast Fourier transform of the USXR signals is then taken, in order to precisely find the frequency of the dominant perturbation. This frequency is used to assign a series of times to the calculations of the different mode-detector phase, allowing the direct comparison of the simulation to data in Fig. 9.

The Princeton Plasma Physics Laboratory is operated
by Princeton University under contract
with the U.S. Department of Energy.

Information Services
Princeton Plasma Physics Laboratory
P.O. Box 451
Princeton, NJ 08543

Phone: 609-243-2245
Fax: 609-243-2751
e-mail: pppl_info@pppl.gov
Internet Address: http://www.pppl.gov